Title
A STUDY OF CHARGE, ENERGY AND ANGULAR MOMENTUM TRANSFER IN THE 56Fe + 197Au AND 56pe + 107,109Ag REACTIONS AT 7.2 AND 8.3 Mev/NUCLEON

Author
Wozniak, G.J.

Publication Date
1982-09-01

Lawrence Berkeley Laboratory
UNIVERSITY OF CALIFORNIA

Submitted to Nuclear Physics

A STUDY OF CHARGE, ENERGY AND ANGULAR MOMENTUM TRANSFER IN THE $^{56}Fe + ^{197}Au$ AND $^{56}Fe + ^{107,109}Ag$ REACTIONS AT 7.2 AND 8.3 Mev/NUCLEON

G.J. Wozniak, G.J. Mathews, R.P. Schmitt, R. Regimbart, H. Hübel, R.M. Diamond, and L.G. Moretto

September 1982

Prepared for the U.S. Department of Energy under Contract DE-AC03-76SF00098

LBL-9461

A STUDY OF CHARGE, ENERGY AND ANGULAR MOMENTUM TRANSFER IN THE $^{56}Fe + ^{197}Au$ AND $^{56}Fe + ^{107,109}Ag$ REACTIONS AT 7.2 AND 8.3 MeV/NUCLEON

G.J. Wozniak, G.J. Mathews, R.P. Schmitt, R. Regimbart, H. Hübel,
R.M. Diamond, and L.G. Moretto

Nuclear Science Division
Lawrence Berkeley Laboratory
University of California
Berkeley, California 94720

This work was supported by the Director, Office of Energy Research, Division of Nuclear Physics of the Office of High Energy and Nuclear Physics and by Nuclear Sciences of the Basic Energy Sciences Program of the U.S. Department of Energy under Contract DE-AC03-76SF00098.

A STUDY OF CHARGE, ENERGY AND ANGULAR MOMENTUM TRANSFER IN THE $^{56}Fe + ^{197}Au$ AND $^{56}Fe + ^{107,109}Ag$ REACTIONS AT 7.2 AND 8.3 MeV/NUCLEON*

G. J. Wozniak, G. J. Mathews,[a] R. P. Schmitt,[b] R. Regimbart,[c] H. Hübel,[d] R. M. Diamond, and L. G. Moretto

Nuclear Science Division
Lawrence Berkeley Laboratory
University of California
Berkeley, California 94720

Abstract

Kinetic energy spectra, charge and angular distributions have been measured for thirty elements produced in the reactions of 401 and 460 MeV $^{56}Fe + ^{197}Au$ and in the reaction of 470 MeV $^{56}Fe + ^{107,109}Ag$. In addition, γ-ray multiplicities were measured at the 470 MeV bombarding energy for both targets at a limited number of angles. The charge distributions for the deep-inelastic component of these systems increase monotonically with atomic number in the measured angular range, whereas, those for the quasielastic component are skewed toward Z-values below the projectile. The angular distributions for the Fe-induced reactions show a smooth evolution from a side-peaked to forward-peaked distributions with increasing mass transfer. This side peak is more intense and more persistent for mass transfers from the projectile to the target. In the quasielastic region the γ-ray multiplicity is observed to increase almost linearly with decreasing Q-value whereas for large negative Q-values it is essentially constant and independent of the exit channel mass asymmetry. Finally, angular distributions, angle-integrated charge distributions and M_γ have been compared with a diffusion model in which the dynamics of shape evolution, N/Z equilibration, angular momentum and energy exchange occur via one-body forces.

NUCLEAR REACTIONS: $^{197}Au(^{56}Fe,Z)$, $^{nat}Ag(^{56}Fe,Z)$, E = 401, 460, 470 MeV; measured σ (E, Z, θ), γ-ray multiplicity for $13 \leq Z \leq 39$. Theoretical interpretation based on a diffusion model.

---

* This work was done with support from the U. S. Department of Energy.

a) Permanent address: University of California, Lawrence Livermore National Laboratory, Livermore, California 94550.

b) Present address: Department of Chemistry and Cyclotron Institute, Texas A & M University, College Station, Texas 77843.

c) Present address: Laboratoire de Physique Corpusculaire Université de Caen, 1400 Caen, France.

d) Permanent address: Institut fur Strahlen und Kernphysik, University of Bonn, Nussallee 14-16, D-5300 Bonn, Germany.

1. Introduction

When two massive heavy ions approach each other, they must overcome both Coulomb and centrifugal barriers to make contact. If the Coulomb and centrifugal fields are sufficiently small, the two nuclei can fuse, forming a compound nucleus. However, if the dynamics are dominated by Coulomb and centrifugal effects, the nuclei, after interacting for a short time, will instead separate. These latter, deep inelastic, collisions occur for a wide range of projectile-target combinations at a few MeV per nucleon over the Coulomb barrier.

In the last decade, extensive studies[1–6] have shown that the primary deep inelastic collision process is essentially binary in nature and that the primary fragments de-excite largely through the evaporation of light particles (n,p,α) and γ-rays. The final kinetic energies of the products range from nearly elastic energies down to the Coulomb interaction energy between highly deformed fragments. Nucleon exchange between the two interacting fragments yields a distribution of product masses. This mass transfer process is controlled by both the interaction time and by the potential energy of the dinuclear system. In addition, angular momentum is transferred from relative orbital motion to the intrinsic spin of the two primary fragments.

Although early studies of deep inelastic collisions were performed with Ar-induced reactions,[7] more recently extensive studies have investigated the bombarding energy and entrance-channel-asymmetry dependence of Kr- and Xe-induced reactions.[2,3,6,8–17] In addition, many model calculations[18–25] have been performed to explain the data from these heavy systems. In contrast, relatively few systematic studies of Fe-induced reactions have been reported.[26-28] In this paper, we report on the kinetic energy spectra, the charge and angular distributions and the transfer of angular momentum in Fe-induced reactions. Diffusion model calculations[29] of the charge and angular distributions as well as the γ-ray multiplicities (M_γ) are also presented.

A brief description of the experimental technique is given in Section 2. Section 3 contains a discussion of the experimental kinetic energy, charge and angular distributions. In Section 4, the γ-ray multiplicity data are considered. A brief description of the diffusion model is given in Section 5 and in Section 6 a comparison of the model calculations and the experimental data is presented.

2. Experimental Technique

2.1. Procedure

Beams of 401, 460 and 470 MeV ^{56}Fe from the Lawrence Berkeley Laboratory SuperHILAC were used to bombard natural, self-supporting targets of $^{107,109}Ag$ and ^{197}Au. The experimental setups for both the singles and coincidence measurements have been described in detail elsewhere[8,10] and will be only briefly outlined here. The atomic number (Z), energy, and lab angle of the reaction products were measured with ΔE-E telescopes. The Z-resolution of this ΔE-E telescope (which consists of a gas ionization ΔE-counter and a solid-state E-counter) is illustrated in fig. 1. The number of events detected in bins 0.2 Z units wide is plotted for products from the reaction of 460 MeV $^{56}Fe + {}^{197}Au$ at 30^{o} over the range from Z = 10 to 40. The peak-to-valley ratio between adjacent elements is generally better than 3/1 below the projectile (Z = 26) and 2/1 from $27 < Z \lesssim 40$.

Gamma-ray multiplicities were also measured at one bombarding energy, 470 MeV. The γ-rays were detected in a multiplicity filter which consisted of six 7.6 cm x 7.6 cm NaI detectors mounted at 45^{o} above the reaction plane. Lead sheets 1.9 cm thick were placed between each counter to reduce Compton scattering into adjacent counters. The γ-ray efficiency of the multiplicity filter was measured for several γ-ray energies with ^{60}Co and ^{207}Bi sources utilizing a seventh NaI detector as a trigger counter. The six NaI detectors were placed at a distance of 15.5 cm from the target in order to obtain a large γ-ray detection efficiency. The summing of prompt γ-rays (from the same reaction event) in a single NaI counter was corrected for in the analysis.[30] Since the flight path of 15.5 cm was insufficient to separate neutrons from γ-rays by their time-of-flight, two additional NaI detectors were placed at a distance of 60 cm to estimate the neutron contamination of the multiplicity filter events. From these time spectra and from the ratio of the neutron to γ-ray detection efficiency ($\Omega_n/\Omega_\gamma \sim 0.1$), it was estimated that the neutron events increased $\langle M_\gamma \rangle$ by less than 10 percent.

Standard NIM electronics were utilized to process the signals from the Z-telescopes and the multiplicity filter. Z-singles events were defined by a slow coincidence between the ΔE and E single channel analyzers of the Z-telescope. Particle-γ coincidence events were established by a fast coincidence (2τ = 30 ns) between the output of the constant fraction discriminator (CFD) of the E detector and each CFD of the NaI array. If this coincidence requirement was met, each NaI logic signal was fed into a box which produced an output proportional to the number of NaI detectors which had fired. (To discriminate against X-rays in the NaI detectors, the lower threshold of the CFDs was set at 100 keV.) The analogue signals from both singles and coincidence events were digitized and written onto magnetic tape with a Mod Comp IV computer for subsequent off-line analysis.

3. Experimental Results

In this section laboratory energy spectra, charge and angular distributions are presented for approximately 30 individually identified elements. The energy dependence of the charge and angular distributions is also described.

3.1. Kinetic Energy Spectra

The energy calibration scheme for the Z-telescopes has previously been described in Ref. 8. The measured lab energies of the detected fragments were corrected for losses in the target, Z-telescope windows, and the dead layer of the solid-state counter using polynomial fits to the Northcliffe and Schilling range-energy data.[31] Additional corrections were made for the pulse-height defect[32] in the solid-state counter. The relative energies should be reliable to approximately 1 percent. Nevertheless, because of uncertainties in the absolute beam energy and in the above corrections, the absolute laboratory energy of a fragment could be in error by up to 2 percent.

To give an overview of the distribution of the reaction cross section in energy and mass asymmetry, two dimensional-contour diagrams of the lab energy vs the Z of the detected fragment were constructed. Products detected at 40^o from the reaction 470 MeV ^{56}Fe + ^{197}Au are shown in Fig. 2. The nearly horizontal ridge which lies between 100 and 300 MeV and stretches from Z = 10 to 40 comprises the deep-inelastic (DI) component. The quasielastic (QE) component shows up as a nearly vertical ridge extending above 300 MeV around Z = 26. Elements far removed from the projectile contain only DI events and have relatively narrow energy distributions, whereas atomic numbers near the projectile have very broad energy distributions, exhibiting a continuous energy relaxation from near beam energies down to the Coulomb barrier. One should note that the very low-energy ridge for Z-values between 30 and 40 actually corresponds to much heavier fragments which have just barely penetrated the ΔE detector, which are, therefore, misidentified in Fig. 2. In addition, for low energies the vertical ridge at Z = 26 is due to slit scattering of the projectile. These events were removed in later stages of the data analysis.

Although the deep-inelastic ridge is nearly constant in energy for Z-values greater than 26, there is a steady decrease for lower Z values. This decrease reflects the smaller Coulomb energies associated with larger mass asymmetries. Another intriguing feature is the sloping of the QE ridge towards smaller Z-values. This preference for the transfer of charge from the projectile to the target in the QE region, has also been observed in the $^{56}Fe + ^{165}Ho$ system.[28] While this skewing of the QE yield to Z-values below the projectile Z was not observed in Kr-induced[8-10,14] reactions at similar energies above the barrier, this feature has been seen at higher bombarding energies[17] and also in Ar-induced reactions.[7] In the above contour diagram which was taken at an angle near the grazing angle, both QE and DI ridges are present. As expected, contour diagrams from data obtained behind the grazing angle exhibit only the DI ridge.

The laboratory energy spectra for each element were obtained from the two dimensional ΔE-E maps by setting gates around each element ridge. These lab spectra were transformed to the c.m. system by assuming charge-equilibrated,[33] pre-evaporative masses. The effect of light particle evaporation (n, p, and α) on the fragment masses and energies was neglected unless otherwise noted. Whenever a distinct DI component was observed in the c.m. energy spectra, its mean value and width were extracted.

Extracted mean values and FWHMs averaged over the angular range of measurements where the DI component was clearly identified are presented in Fig. 3. The "error bars" represent one standard deviation from the average value. For comparison, the solid curve corresponds to the calculated* Coulomb repulsion energies for two touching spheres. The mean energies are somewhat lower than the calculated energies, a difference which increases with increasing Z-value. This is probably due to the effects of particle evaporation and deformation of the fragments. One should note that the average energy of the DI component (uncorrected for particle emission) is essentially independent of bombarding energy. This feature has been observed previously[34] in the similar system $^{63}Cu + ^{197}Au$. However, this behavior is not expected to hold over a very large range of bombarding energies. Eventually higher angular momenta should produce higher fragment kinetic energies (before evaporation). Some evidence for this effect has been seen in Kr-induced reactions.[14] One should also note that the values of the FWHM for the DI component are significantly larger at the higher bombarding energy. This increase could partially arise

---

*$R = 1.225(A_1^{1/3} + A_2^{1/3}) + 2.$

from the larger number of light particles emitted from the "hotter" DI fragments formed at the higher bombarding energy. It is also likely that the higher temperature of the intermediate complex also leads to a greater width due to the enhanced excitation of shape fluctuations.[35]

In Fig. 3b values of the mean c.m. energies and FWHMs are presented for the DI component measured for the 470 MeV $^{56}Fe + ^{107,109}Ag$ reaction. As in the $^{56}Fe + ^{197}Au$ system, the mean c.m. energies fall slightly below but roughly parallel to the calculated Coulomb energies. The values of the FWHM are relatively independent of Z and are similar in magnitude (30-40 MeV) to those for the $^{56}Fe + ^{197}Au$ system (see Fig. 3a). Similar values were also observed in Kr-induced reactions.[8,9,14]

3.2. Charge Distributions

Laboratory charge distributions integrated over both the QE and DI components are presented in Figs. 4 and 5. For the Au bombardments the most striking feature is the intense peak which is highly skewed towards Z values below that of the projectile. This peak persists over a large laboratory angular range for both the 401 MeV and the 460 MeV data. The peak, which is broadest at the most forward angles, increases in magnitude and narrows for intermediate angles, and disappears at the most backward angles.

The angular dependence of the width of this peak, which is composed mainly of QE events (see Fig. 2), can be explained in terms of the ℓ-dependence of the interaction time. The largest ℓ-waves correspond to the shortest interaction times, which characterize the yield close to the grazing angle. Since there is little time for mass transfer, these Z-distributions are rather sharp. At more forward angles (i.e., 30° in Fig. 4a), the QE yield is produced by intermediate ℓ-waves as evidenced by the observed lower kinetic energies. Since more time is required for the intermediate complex to rotate to more forward angles before decaying, more mass transfer can occur, broadening the Z-distribution. The yield at very backward angles corresponds to the lowest ℓ-waves and hence the longest interaction times. At very backward angles (i.e., 70° in Fig. 4a), the Z-distributions seem to approach the equilibrium limit, which peaks at symmetry ($Z = 52$). For angles slightly backward of the grazing (i.e., 60° in Fig. 4a), the QE peak appears to be sitting on the slope of the steeply rising nearly equilibrated component.

One striking feature evident in Fig. 4 is the pronounced skewing of the QE peak towards Z-values below that of the projectile. This shift of the mean value by 1 to 2 Z-units below Fe is likely to be associated with the rapid equilibration of the neutron-to-proton ratio of the interacting system.[29] Because ^{56}Fe has an A/Z ratio (2.15) which is substantially lower than that of ^{197}Au (2.49), the neutron-to-proton ratios can be most quickly equilibrated by transferring protons from the projectile to the target. Recent measurements[26,27] with discrete Z and A resolution of Fe-like fragments produced in DI collisions show that proton stripping to the target is favored, and that the time scale for N/Z equilibration is comparable to that of the energy damping process. The charge distributions of the ^{56}Fe + $^{107,109}Ag$ system (see Fig. 5) show much less skewing of the QE peak. This perhaps reflects the fact that the A/Z ratio of the projectile (2.15) and target (2.30) are more comparable. Since this lighter system was studied at a substantially larger energy over the barrier E/B = 2.20, its grazing angle is considerably smaller. Thus behind 20^o, the Z-distributions show only an "equilibrated" DI component which peaks near symmetry (Z = 36).

To illustrate how the total reaction yield is distributed along the charge asymmetry degree of freedom, the experimental Z-distributions were integrated over energy and angle by extrapolating over the measured $(d\sigma/d\theta)_{c.m.}$ to 0° and to 180°. The resulting total charge distributions for the Fe + Au systems are shown in Fig. 6. Although the yield increases with bombarding energy, the overall shapes at both energies are very similar. At the higher bombarding energy, the large increase in yield for Z-values less than 26 could possibly be due to the onset of 3-body processes similar to those observed by Olmi et al.,[17] in high energy Kr reactions. An alternative explanation is that this large increase in yield is the result of the larger temperature which increases the spreading to larger asymmetries in a diffusive mass transfer process. Similar behavior has been observed in low energy Kr-induced reactions.[14]

Figure 2 illustrated the coupling of the energy dissipation process with the relaxation along the mass asymmetry degree of freedom. To investigate the dependence of the measured Z-distributions on the degree of energy damping in more detail, angle-integrated charge distributions have been constructed for various energy windows (see Fig. 7). As described in Refs. 8 and 9, these distributions have been constructed by making cuts (20 MeV wide) in the c.m. energy spectra parallel to the mean relaxed energy (approximately parallel to the Coulomb energy) as defined by the data in Fig. 3. The lowest energies in Fig. 7 correspond to the lowest bin numbers. The relaxed peak is roughly centered in bin 7.

The angle-integrated charge distributions exhibit a dramatic dependence on energy damping for both bombarding energies. In Fig. 7b one sees that the distribution is very narrow and is peaked at about the projectile Z-value when the energy damping is small (bins 15 and 14). As the degree of energy damping is increased (bins 13–9), the distribution broadens and drifts to lower Z-values. For fully damped events this peak abruptly disappears and a rapid transition occurs to very broad distributions with mean values substantially above the projectile Z-value. This drift of the peak toward lower Z-values with increasing energy damping is consistent with the equilibration of the neutron-to-proton ratio during the short lived QE collisions. For the longer lived fully damped collisions, one observes Z-distributions more closely resembling an equilibrium distribution.

3.3. Angular Distributions

Center-of-mass angular distributions for atomic numbers between 13 ($\Delta Z = -13$) and 39 ($\Delta Z = +13$) are presented in Fig. 8. Because of background from slit scattering, data for the projectile ($Z = 26$) have been omitted. Distributions for the same net charge transfer to and from the projectile (i.e., $\pm \Delta Z$) are shown in adjacent columns. The amount of charge transferred increases from 1 to 13 down the columns. For both bombarding energies, one observes the evolution from side peaked to forward peaked angular distributions with increasing charge transfer. (For comparison, a $1/\sin\theta$ angular distribution is shown at the bottom of the 2nd column.) For the higher bombarding energy the evolution towards forward peaking proceeds faster, presumably because the grazing angle is smaller for the larger bombarding energy. More striking is the marked asymmetry in this evolution for charge transfer to and from the projectile, a feature observed at both bombarding energies. For Z-values larger than 26 ($\Delta Z > 0$), the side peak is very weak and quickly disappears for larger charge transfers. For Z-values less than 26 ($\Delta Z < 0$), the side peak is much more intense and persists for much larger charge transfers.

The evolution from side- to forward-peaked distributions has been explained[2,8] in terms of a diffusion-controlled time delay. On the average, small charge transfers require less time than larger ones in a diffusion process. Since small charge transfers populate elements near the projectile, the mean lifetime is short, resulting in side-peaked angular distributions. For larger charge transfers, the longer average lifetimes allow the intermediate complex to rotate more before decaying. This produces forward-peaked angular distributions. The fact that the evolution proceeds more rapidly at the higher bombarding energy is probably due to the larger orbital velocity of the intermediate complex and the smaller angular distance (more forward grazing angle) through which it must rotate to reach 0^{o}.

The large difference in the rate of evolution of the side peak for $\Delta Z > 0$ and $\Delta Z < 0$ can be better understood by examining the angular distributions as a function of Q-value. At both bombarding energies (see Figs. 9 and 10) the side peak is clearly seen to be associated with the partially damped events, and, in general, the intensity of the side peak decreases with increasing energy dissipation. Since the Z-values above the projectile have a smaller fraction of the partially damped events, the side peak for the energy-integrated angular distribution is relatively weak. One should note that for the lowest energy bins both the shape and magnitude of the cross sections are very similar for the same amount of charge transfer to or from the projectile. Again one notes that the evolution from side-peaked to forward-peaked angular distributions is more complete at the higher bombarding energy, probably because of the higher temperature, smaller grazing angle and larger range of energy losses.

4. Gamma-Ray Multiplicity Data

Further insight into the heavy-ion reaction mechanism can be obtained by studying the angular momentum transfer. In a simple macroscopic model the initial orbital angular momentum is transformed into fragment spin by the tangential component of the friction tensor. The total angular momentum, $\Delta\ell$, transferred into intrinsic rotation depends on the range of partial waves involved, the interaction time, the initial asymmetry of the system, and the rate of mass transfer. Thus correlations of $\Delta\ell$ with the degree of energy damping and the relaxation of the mass-asymmetry degree of freedom for Fe-induced reactions can test various models of the energy dissipation and mass transfer process. It is also interesting to see if the angular momentum fractionation promoted by the ridge-line potential energy, which was observed in Kr-induced reactions[15,18] is evident in Fe-induced reactions.

To investigate angular momentum transfer, we have measured the average number of γ-rays (M_γ) emitted during the de-excitation of the two excited fragments. If the multipolarity of these γ-rays were known, it would be possible to determine the angular momentum carried away by the γ-rays. Compound nucleus studies[36-38] of intermediate mass nuclei have shown that the fragment spin is carried off mainly by the γ-ray cascade and that this cascade consists primarily of stretched E2 transitions. By analogy, the total spin of the two fragments ($I_1 + I_2 = \Delta\ell$) produced in the DI collision can be related to the γ-ray multiplicity (neglecting angular momentum loss by particle emission) by the expression:

$$M_\gamma = 1/2(I_1 + I_2) + 2\alpha \quad , \tag{4-1}$$

where α is the number of statistical γ-rays emitted per fragment as it decays to the yrast band. Both compound-nucleus and DI studies with heavy-ion reactions[36-39] indicate that α ranges from 2 to 4 depending upon the nucleus.

In the following subsections the energy, angular and mass dependence of M_γ will be discussed for the systems 470 MeV ^{56}Fe + $^{107,109}Ag(\ell_{max} = 216\hbar)$ and 470 MeV ^{56}Fe + $^{197}Au(\ell_{max} = 246\hbar)$. These two systems are interesting both because relatively large amounts of angular momentum are involved and because they correspond to different entrance-channel asymmetries.

4.1. Energy Dependence of M_γ

The dependence of M_γ on kinetic energy is shown in Fig. 11 for the system 470 MeV ^{56}Fe + ^{197}Au at $\theta_{lab} = 40^0$. For three Z-bins, M_γ is plotted against the total exit-channel kinetic energy (TKE) corrected for neutron evaporation. Let us first concentrate on the bin for Z = 21-30 (part b) where a continuous range of energy damping is observed. In part b a very strong correlation is observed between M_γ and the degree of energy damping. M_γ first rises steadily with decreasing TKE, then levels off for TKE values between 150-250 MeV and finally decreases by ~30 percent for very small (~150 MeV) TKE. For the two Z-bins far removed from the projectile (corresponding to large mass transfers), where only a fully relaxed energy component is observed, M_γ has a constant value of ~20, with perhaps a slight falloff at the smallest TKE.

For the system 470 MeV ^{56}Fe + $^{107,109}Ag$, M_γ averaged over the angular range (θ_{lab} = 20-80^o), is presented in Fig. 12. Although the magnitude of M_γ is slightly lower than that obtained with Au (as would be expected from the smaller ℓ_{max} value), a very similar pattern is observed. One should note that the Fe + Ag data extend to lower TKE than the Fe + Au data because of the smaller Coulomb energy of the former system.

The correlation of M_γ with the degree of energy damping can be interpreted as follows. The initial rapid increase of M_γ with decreasing TKE is due to the rapid transfer of angular momentum, which occurs as the energy of relative motion is being equilibrated.[39] Although the angular momentum of the incident partial wave, ℓ, decreases with decreasing TKE, both the interaction time and the number of particle transfers increase, allowing a larger fraction of the entrance channel angular momentum to be converted into intrinsic spin. When rigid rotation of the dinuclear system[10,40,41] is reached in the DI region, the maximum fraction of the entrance channel angular momentum is converted into intrinsic spin. Thus in this simple picture M_r should reach a maximum in the DI region and then decrease for smaller values of TKE. The fact that M_γ is relatively constant over the DI region indicates the presence of other processes[39,42,43] (e.g., shape fluctuations and thermally excited bending and wriggling modes), which can generate intrinsic angular momentum in the fragments and smear the simple correlation between kinetic energy and angular momentum. The observed gradual decrease of M_γ in the region of very small TKE may also be due to the increased probability of charge-particle emission which can carry off substantial amounts of angular momentum.

4.2. Dependence of M_γ on Mass Transfer and on Angle

In Kr-induced reactions M_γ depends strongly on the exit channel asymmetry for partially damped events and weakly for fully damped events.[15,16,18] For Fe-induced reactions this behavior is also readily apparent in Figs. 13 and 14, where energy-integrated M_γ are shown as a function of exit channel asymmetry. Data obtained near the grazing angles for both the Fe + Au (Fig. 13) and the Fe + Ag (Fig. 14a) systems show a strong dip at the projectile Z-value which is caused by the substantial QE component. At angles of 40° and larger where only fully damped events are observed in the Fe + Ag system, M_γ is essentially independent of Z.

The independence of M_γ (on mass asymmetry for fully relaxed events) observed in the above Fe data and in Kr-induced reactions,[15,16,18] is in marked contrast to results obtained for light systems like 175 MeV ^{20}Ne + Ag. For such light systems a strong dependence of M_γ on mass asymmetry is observed[40,41] which is indicative of rigid rotation. However, the sub-Coulomb kinetic energies of the products from the Kr-induced reactions also imply that rigid rotation is achieved. Unlike light systems, the DI reactions induced by Kr occur within a very large ℓ-window. Because of this large ℓ-window, different ℓ-waves can populate different mass asymmetries producing an ℓ-fractionation[15] as borne out by diffusion model calculations.[18] Angular momentum fractionation arises because both the intermediate complex lifetime and the potential energy surface controlling the mass transfer are strongly ℓ-dependent. Since the interaction time increases with decreasing angular momenta, more mass transfer (on the average) occurs for low ℓ-waves. A similar effect results from the decreasing steepness of the slope of the driving potential for diffusion with decreasing ℓ-waves.[42] For DI reactions induced by very heavy projectiles both of these ℓ-fractionation effects tend to compensate any increase of M_γ with increasing asymmetry.

For the Fe + Ag system, M_γ decreases with increasing lab angle, which may be interpreted as evidence for orbiting in this system. The angles backward of the grazing angle seem to be populated predominantly by low ℓ-waves. These ℓ-waves lead to dinuclear systems with relatively long lifetimes (as evidenced by the equilibrated Z-distribution); however, the low angular velocities do not permit these systems to rotate through large angles.

5.1 Model

As we have seen in the previous sections, a number of interesting effects occur in Fe-induced reactions which correlate with the mass transfer process. Hence, it is desirable to compare these data with detailed model calculations based on the nucleon-exchange process. The evolution of the dinuclear system along the mass asymmetry coordinate can be described as a diffusive process. Recently, the diffusion model of Moretto and Sventek[19], has been extended by Mathews et al.[29] to include the effect of N/Z equilibration and the influence of the shape evolution of the system. In particular, this diffusion model attempts to eliminate some of the free parameters associated with the collision dynamics.

The driving force for diffusion is determined by the total effective potential energy of the ion-ion complex. In Fig. 15 the calculated total effective potential energy, as a function of asymmetry (labelled by the atomic number of one fragment), are presented for the $^{56}Fe + ^{197}Au$ reaction at two bombarding energies and for several ℓ-waves ($\ell = 0$, ℓ_{rms} and ℓ_{max}). The potential energy has been calculated relative to the injection point (Z = 26) along the valley of (N/Z) equilibrium. These potentials assume rigid rotation of the complex at an average overlap distance calculated from the dynamics [29] and should represent the path along which the system diffuses after (N/Z) equilibrium has resulted. For the high partial waves, the large negative slope of the potential at the injection point gives rise to a substantial driving force toward symmetry. Therefore, on the basis of these potential energies alone, the Z-values above the projectile should be preferentially populated, while those below should be rarely populated by these partial waves. Even for the very lowest ℓ-waves there is still a driving force toward symmetry, but it is much weaker. Thus, these partial waves might populate asymmetries substantially above and below the entrance channel asymmetry. For the two bombarding energies, the potential energy curves are very similar.

In addition to the relatively slow evolution[2] of the system along the mass-asymmetry coordinate, however, a more rapid equilibration of the N/Z ratio of the system should occur.[1,26,27] This means that even though the mass asymmetry of the system can probably be characterized by the Z of one of the fragments, there is important drift and dispersion in the Z distribution due to the separate equilibration of the N and Z degrees of freedom. This effect was introduced in the model[29] by solving a Fokker-Planck equation for an harmonic potential along the Z coordinate at fixed mass asymmetry.

To describe the shape evolution of the system, a cylindrical neck was assumed to form between the two ions.[44] Neglecting volume conservation and the Coulomb energy of the cylinder, the contribution of the neck to the potential energy of the system is just the difference between the surface energy of the cylinder and the surface energy of the neck area of the two interacting ions. The neck degree of freedom also affects the driving potential for diffusion, the form factor, and the lifetime of the interacting system.

Fig. 16 shows the calculated interaction time as a function of the incoming partial wave for the ^{56}Fe + ^{197}Au system at two bombarding energies with and without the neck degree of freedom. The lifetime distributions are quite similar for both bombarding energies. Introducing the neck degree of freedom dramatically increases the lifetime for low and intermediate partial waves. The neck holds the window between the fragments open for a longer time. One should note that for this system, the formation of a neck is not sufficient to trap the two ions, thus no complete fusion is predicted in this model. The bifurcation of the two curves (into neck and no neck curves) corresponds to collisions which just penetrate to the geometric limit for neck formation, i.e., contact point of the two quarter-density radii.

6. Discussion

In this section the diffusion model results are compared with the data. Of course, by adjusting various parameters of the model, better fits could be obtained.[25] The approach we have adopted here, however, has been to eliminate free parameters associated with the collision dynamics. The differences between the model predictions and the data should thus highlight interesting features of the reaction process.

6.1 Charge distributions

It is instructive to first compare the theoretical and experimental angle- and energy-integrated charge distributions. By comparing Z-distributions with the model, some of the sensitivity to details of the dynamics is removed. Thus, the integrated charge distributions may be a good indicator of how well the one-body transport model describes the data independently of the dynamics (which are treated here only in an average, schematic way).

The calculated and experimental total charge distributions for the Fe + Au system are presented in Fig. 17. For small mass transfers, the calculations reproduce the yield around the projectile and in particular the skewing of this yield to smaller Z-values. This success is due primarily to the inclusion of the N/Z equilibration process in the model. It is also encouraging that the longer lifetimes associated with neck formation lead to yields more consistent with the data for Z-values above the projectile. However, for the low Z-values, the model underproduces the yields, and, moreover, shows a trend with bombarding energy which is opposite to that observed in the data (i.e., a narrower rather than a broader distribution at higher bombarding energy). It was found that changing the lifetime, the variance of the lifetime and the critical distance for the onset of neck formation did not substantially improve the agreement with the data. This implies that the real driving potentials (Fig. 15) for diffusive mass transfer are perhaps not as steep at the entrance channel asymmetry as those utilized in the calculations. This conclusion is indicated by the "neck" calculations which dramatically increase the mean lifetimes for intermediate and low ℓ-waves and cause a large shift of the yield to larger Z-values relative to the "no-neck" calculations. With the large negative slope of the driving potential at the injection point, increasing either the lifetime or the variance of the lifetime distribution results in a depletion of yield for low Z-values and an enhanced yield for larger Z-values. This result may indicate the need for more shape degrees of freedom than allowed for in the averaged dynamics of this model. It may be necessary to follow the actual evolution of the potential (and driving forces) during the collision.

6.2 Gamma-ray multiplicities

To gain further insight into the ℓ-fractionation along the mass asymmetry coordinate, we have compared the transferred angular momentum as calculated by the model with energy-integrated M_γ for different exit channel asymmetries. The transformation from the calculated fragment spins to M_γ utilized Equation 4-1. The number of statistical γ-rays per fragment α was taken to be 3. Because there is some uncertainty in this value, caution must be exercised in comparing the absolute values of the calculated and measured multiplicities.

In Figs. 13 and 14, a comparison is presented between the data and the calculations (with neck) for the energy-integrated M_γ as a function of mass asymmetry. For angles near the grazing angle and for small mass transfers, the sharp asymmetric dip at Z = 26 is nicely reproduced for both the Au and Ag data at 40° and 20°, respectively. For larger mass transfers the agreement with the data is poorer. For Z-values between 12 and 22, the calculations slightly underpredict M_γ whereas above Z = 33 the calculations overpredict M_γ. For the more backward angle Ag data, the calculations generally overpredict the magnitude of M_γ. The above comparisons indicate that in the model too much of the yield from intermediate ℓ-waves is drifting toward symmetry due to potential surfaces which are too steep. The near discontinuity in the calculated values of M_γ at Z = 20 for the Fe + Au system arises because the Z-values below 20 are populated only by low ℓ-waves whereas the Z-values above Z = 20 are populated by the highest ℓ-waves. A calculation with a flatter potential-energy surface would produce a larger yield for atomic numbers below the projectile and a larger and smoother M_γ.

6.3 Angular Distributions

The most sensitive test of the model dynamics involves a comparison between the calculated and experimental angular distributions for individual Z-values. In Fig. 18, this comparison is made for several representative Z-values (from the Fe + Au system). For small mass transfers, the agreement between the data and the calculations is reasonable. However, for large mass transfers, the calculations diverge significantly from the data. In general, the calculations including the neck degree of freedom, are in better agreement with the data. The longer lifetime for small partial waves better reproduces the strong decrease in yield behind the grazing angle which is observed in the data. The magnitude of the side peak for Z-values above the projectile, however, is too intense and occurs at too large an angle. This effect is related to the excessive drift towards symmetry observed for the charge distributions. The narrow side peak observed in the data could perhaps be reproduced with a narrower lifetime distribution for short lifetime collisions as recent dynamical simulation studies suggest.[45] (In the above calculations, a gaussian lifetime distribution was assumed for each partial wave with a variance equal to 1.5 times the mean interaction time.)

In Fig. 19 are shown the angular distributions of several representative Z-values for the Fe + Ag system. For all mass transfers forward of 90^{o}, the agreement between the data and the calculations (with neck degree of freedom) is reasonable. The strong forward peak in the data and the rate of fall off with increasing angle are nicely reproduced by the calculations. The agreement at large angles ($>90^{\circ}$) is poor. While the calculations indicate an increase in yield at large angles, the data are consistent with a smooth decrease in cross section with increasing angle.

7. Conclusions

In summary, kinetic energy spectra, charge and angular distributions, as well as γ-ray multiplicities were presented for ^{56}Fe-induced reactions with a ^{nat}Ag and a ^{197}Au target at two bombarding energies. In the quasi-elastic region, the product Z-distributions, from the $^{56}Fe + ^{197}Au$ system, are skewed toward Z-values below that of the projectile. Diffusion model calculations indicate that this skewing is probably the result of the N/Z equilibration of the system. For the $^{56}Fe + ^{197}Au$ system, an evolution from side to forward peaked angular distributions is observed with increasing charge transfer. This evolution is not symmetric for charge transfers to and from the projectile. For products lighter than the projectile, the side peak is more intense and persists for much larger charge transfers. This pattern of the angular distributions is more similar to Ar-induced than Kr-induced reactions.

In the quasi-elastic region, the large increase of the γ-ray multiplicity with increasing energy loss implies a good correlation of energy loss and ℓ-value. In the deep-inelastic region, the subsequent saturation of the γ-ray multiplicity indicates a poor correlation. The γ-ray multiplicitiy in the deep-inelastic region was observed to be independent of the mass asymmetry of the system which indicates an ℓ-fractionation effect similar to that observed for Kr-induced reactions. However, the steady decrease of the γ-ray multiplicity with increasing angle implies that the deflection function for the Fe + Ag system is not as strongly focussed as those for Kr-induced reactions.

Diffusion model calculations were performed with a model which incorporated the collision dynamics, the N/Z equilibration and the shape evolution of the dinuclear system. For the Fe + Ag system reasonable agreement was observed between the calculations and the experimental γ-ray multiplicities and the angular distributions. For the Fe + Au system the model does well for Z values close to the projectile and poorly for Z values substantially larger or smaller than the projectile. A detailed comparison of the data with the model calculations indicates a need for improvements in the calculation of the collision dynamics and the ridge-line potential. Work along this line is currently in progress.[45]

This work was supported by the Director, Office of Energy Research, Division of Nuclear Physics of the Office of High Energy and Nuclear Physics and by Nuclear Sciences of the Basic Energy Sciences Program of the U.S. Department of Energy under Contract DE-AC03-76SF00098.

References

1. J. Galin, J. de Phys. 37 Colloq C5 Suppl. No. 11 (1976) 83, and references therein.
2. L. G. Moretto and R. Schmitt, J. de Phys. 37 Colloq C5 Suppl. No. 11 (1976) 109, and references therein.
3. W. U. Schröder and J. R. Huizenga, Ann. Rev. Nucl. Sci. 27 (1977) 465, and references therein.
4. V. V. Volkov, Phys. Rep. 44 (1978) 93, and references therein.
5. M. Lefort and C. Ngô, Ann. Phys. NY3 (1978) 5, and references therein.
6. L. G. Moretto and R. P. Schmitt, Rep. Prog. Phys. 44 (1981) 533.
7. A. G. Artukh, G. F. Gridnev, V. L. Mikheev, V. V. Volkov and J. Wilczynski, Nucl. Phys. A215 (1973) 91.
8. P. Russo, R. P. Schmitt, G. J. Wozniak, R. C. Jared, P. Glässel, B. Cauvin, J. S. Sventek and L. G. Moretto, Nucl. Phys. A281 (1977) 509.
9. R. P. Schmitt, P. Russo, R. Babinet, R. Jared and L. G. Moretto, Nucl. Phys. A279 (1977) 141.
10. L. G. Sobotka, C. C. Hsu, G. J. Wozniak, D. J. Morrissey and L. G. Moretto, Nucl. Phys. A371 (1981) 510.
11. W. W. Wilcke, J. R. Birkelund, A. D. Hoover, J. R. Huizenga, W. U. Schröder, V. E. Viola, Jr., K. L. Wolf, and A. C. Mignerey, Phys. Rev. C22 (1980) 128.
12. H. J. Wollersheim, W. W. Wilcke, J. R. Birkelund, J. R. Huizenga, W. U. Schröder, H. Freiesleben and D. Hilscher, Phys. Rev. C24 (1981) 2114.

13. P. Dyer, M. P. Webb, R. J. Puigh, R. Vanderbosch, T. D. Thomas, and M. S. Zisman, Phys. Rev. C22 (1980) 1509.

14. R. P. Schmitt, Lawrence Berkeley Laboratory Report No. 7168, (Ph.D thesis) May 1978.

15. M. M. Aleonard, G. J. Wozniak, P. Glässel, M. A. Deleplanque, R. M. Diamond, L. G. Moretto, R. P. Schmitt, and F. S. Stephens, Phys. Rev. Lett. 40 (1978) 622.

16. P. R. Christensen, F. Folkmann, Ole Hansen, O. Nathan, N. Trautner, F. Videbaek, S. Y. van der Werf, H. C. Britt, R. P. Chestnut, H. Freiesleben and F. Pühlhofer, Nucl. Phys. A349 (1980) 217.

17. A. Olmi, U. Lynen, J. B. Natowitz, M. Dakowski, P. Doll, A. Gobbi, H. Sann, H. Stelzer, R. Bock, and D. Pelte, Phys. Rev. Lett. 44 (1980) 383.

18. R. Regimbart, A. N. Behkami, G. J. Wozniak, R. P. Schmitt, J. S. Sventek, and L. G. Moretto, Phys. Rev. Lett. 41 (1978) 1355.

19. J. S. Sventek and L. G. Moretto, Phys. Rev. Lett. 40 (1978) 697.

20. Georg Wolschin and Wolfgang Nörenberg. Phys. Rev. Lett 41 (1978) 691.

21. A. Sherman, D. Sperber, M. I. Sobel and J. P. Bondorf, Z. Physik A286 (1978) 11.

22. D. Agassi, C. M. Ko and H. A. Weidenmüller, Phys. Rev. C18 (1978) 223.

23. H. Esbensen, A. Winther, R. A. Broglia and C. H. Dasso, Phys. Rev. Lett. 41 (1978) 296.

24. D. H. E. Gross and K. M. Hartmann, Phys. Rev. C24 (1981) 2526.

25. L. G. Moretto, J. Phys. Soc. Jpn., Suppl. 44 361 (1978).

26. H. Breuer, B. G. Glagola, V. E. Viola, K. L. Wolf, A. C. Mignerey, J. R. Birkelund, D. Hilscher, A. D. Hoover, J. R. Huizenga, W. U. Schröder, and W. W. Wilcke, Phys. Rev. Lett 43 (1979) 191.

27. A. C. Mignerey, V. E. Viola, Jr., H. Breuer, K. L. Wolf, B. G. Glagola, J. R. Birkelund, D. Hilscher, J. R. Huizenga, W. U. Schröder and W. W. Wilcke, Phys. Rev. Lett. 45 (1980) 509.

28. A. D. Hoover, J. R. Birkelund, D. Hilscher, W. U. Schröder, W. W. Wilcke, J. R. Huizenga, H. Breuer, A. C. Mignerey, V. E. Viola, Jr. and K. L. Wolf, Phys. Rev. C25 (1982) 256.

29. G. J. Mathews, J. B. Moulton, G. J. Wozniak, B. Cauvin, R. P. Schmitt, J. S. Sventek and L. G. Moretto, Phys. Rev. C25 (1982) 300.

30. G. B. Hagemann, R. Broda, B. Herskind, M. Ishihara, S. Ogaza, and H. Ryde, Nucl. Phys. A245 166 (1975).

31. L. C. Northcliffe and R. F. Schilling, Nucl. Data Tables A7 (1970) 233.

32. J. B. Moulton, E. J. Stephenson, R. P. Schmitt and G. J. Wozniak, Nucl. Instr. and Meth. 157 (1978) 325.

33. B. Gatty, D. Guerreau, M. Lefort, J. Pouthas, X. Tarrago, J. Galin, B. Cauvin, J. Girard and H. Nifenecker, Z. Phys. A273 (1975) 65.

34. B. Tamain, F. Plasil, C. Ngô, J. Péter, M. Berlanger and F. Hanappe, Phys. Rev. Lett. 36 (1976) 18.

35. L. G. Moretto, Nucl. Phys. A247 (1975) 211.

36. M. A. Deleplanque, Th. Byrski, R. M. Diamond, H. Hübel, F. S. Stephens, B. Herskind and R. Bauer, Phys. Rev. Lett. 41 (1978) 1105.

37. O. Andersen, R. Bauer, G. B. Hagemann, M. L. Halbert, B. Herskind, M. Neiman, H. Oeschler, and H. Ryde, Nucl. Phys. A295 (1978) 163.

38. R. S. Simon, M. V. Banaschik, R. M. Diamond, J. O. Newton and F. S. Stephens, Nucl. Phys. A290 (1977) 253.

39. R. J. McDonald, A. J. Pacheco, G. J. Wozniak, H. H. Bolotin, L. G. Moretto, C. Schück, S. Shih, R. M. Diamond, and F. S. Stephens, Nucl. Phys. A373 (1982) 54.

40. P. Glässel, R. S. Simon, R. M. Diamond, R. C. Jared, I. Y. Lee, L. G. Moretto, J. O. Newton, R. Schmitt, and F. S. Stephens, Phys. Rev. Lett. 38 (1977) 331.

41. J. B. Natowitz, M. N. Namboodiri, P. Kasiraj, R. Eggers, L. Adler, P. Gonthier, C. Cerruti, and T. Allemen, Phys. Rev. Lett. 40 (1978) 751.

42. L. G. Moretto and R. P. Schmitt, Phys. Rev. C21 (1980) 204.

43. R. P. Schmitt and A. J. Pacheco, Nucl. Phys. 379 (1982) 313.

44. W. J. Swiatecki, International School of Nuclear Physics, Erice-Trapani, Sicily, 1979, Report No. LBL-8950.

45. G. J. Mathews, J. Randrup and L. G. Moretto, LBL-10126 (to be submitted to Nucl. Phys. A.).

Figure Captions

Fig. 1. Intensity distribution vs. atomic number of the fragments detected at 30^{0} lab illustrating the discrete Z-resolution attained with the ΔE-E telescopes.

Fig. 2. Contours of laboratory energy (E_3) vs. atomic number Z for products detected at 40^{0} lab for the reaction 470 MeV ^{56}Fe + ^{197}Au. The contours are averaged over 1 Z-unit, therefore the discrete Z-ridges cannot be seen.

Fig. 3. Mean c.m. energies and FWHMs of the DI component observed in the a) ^{56}Fe + ^{197}Au reaction at two bombarding energies: 401 MeV (solid circles), 460 MeV (squares) and b) the 470 MeV ^{56}Fe + ^{107,109}Ag reaction. The FWHM was computed from the second moment of the spectra by assuming a Gaussian peak shape. "Error bars" which correspond to one standard deviation from the mean value, are shown for the 401 and 470 MeV data. They are of similar magnitude for the 460 MeV data. See discussion in text.

Fig. 4. Energy-integrated charge distributions (curves) measured at several lab angles for the a) 401 and b) 460 MeV ^{56}Fe + ^{197}Au reactions. Data points are shown for some representative angles. Statistical error bars are shown only when they exceed the size of the data point. Cross sections for Z = 26 may lie above the smooth curve drawn through the data points because of background contributions from slit scattering and difficulties in subtracting out the low energy tail of the elastic peak.

Fig. 5. Charge distributions for the combined DI and QE components observed in the 470 MeV $^{56}Fe + ^{107,109}Ag$ reaction at several lab angles. See caption of Fig. 4.

Fig. 6. A comparison between the experimental angle-integrated cross section for fragments ($10 \leq Z \leq 40$) produced in the reaction $^{197}Au + ^{56}Fe$ at two-bombarding energies: 401 MeV (solid circles) and 460 MeV (squares). See discussion in text.

Fig. 7. Angle-integrated charge distributions from the a) 401 and b) 460 MeV $^{56}Fe + ^{197}Au$ reaction for various c.m. kinetic energy windows. The bin number multiplied by twenty gives the upper limit of the window in MeV for Z = 26. Bin 7 is approximately centered on the relaxed peak.

Fig. 8. Experimental c.m. angular distributions for elements detected from the ^{197}Au + a) 401 and b) 460 MeV ^{56}Fe reaction. Distributions for the same net charge transfer to ($\Delta Z > 0$) and from ($\Delta Z < 0$) the projectile are shown in adjacent columns. The curves through the data points serve only to guide the eye.

Fig. 9. Experimental c.m. angular distributions for several kinetic energy windows and four selected elements from the ^{197}Au + 401 MeV ^{56}Fe reaction. Bin 7 is approximately centered on the relaxed peak. The curves through the data points serve only to guide the eye.

Fig. 10. Experimental c.m. angular distributions for several kinetic-energy windows and four selected elements from the ^{197}Au + 460 MeV ^{56}Fe reaction. See caption of Fig. 9.

Fig. 11. M_γ vs total kinetic energy (TKE) for the reaction 470 MeV $^{56}Fe + ^{197}Au$ at $\theta_{lab} = 40^0$. The experimental TKE has been corrected for neutron evaporation and averaged over 10 Z-values (a) Z = 11–20, (b) Z = 21–30, (c) Z = 31–40. Only relative errors are shown.

Fig. 12. M_γ vs. TKE for the reaction 470 MeV $^{56}Fe + ^{107,109}Ag$. The experimental data have been averaged over the angular range $20–80^0$ lab. See caption of Fig. 11.

Fig. 13. A comparison of the experimental (symbols) and calculated (line) energy-integrated M_γ for products from the reaction 470 MeV $^{56}Fe + ^{197}Au$ at 40°. Only relative errors are shown.

Fig. 14. A comparison of the experimental (symbols) and calculated (line) energy-integrated M_γ for products from the reaction 470 MeV $^{56}Fe + ^{107,109}Ag$. Only relative errors are shown.

Fig. 15. Calculated total effective liquid-drop potential energy curves as a function of charge asymmetry for the $^{56}Fe + ^{197}Au$ reaction at two bombarding energies for three ℓ-waves. The potential energies have been plotted relative to the entrance channel value.

Fig. 16. Calculated interaction times as a function of the incident partial wave for the $^{56}Fe + ^{197}Au$ system at 401 and 460 MeV with and without the neck degree of freedom.

Fig. 17. A comparison between the experimental angle-integrated cross section (symbols) and diffusion model calculations with (solid lines) and without (dashed lines) the neck degree of freedom for the 401 and 460 MeV ^{56}Fe + ^{197}Au reactions.

Fig. 18. A comparison between experimental (solid line) and calculated c.m. angular distributions with (dashed) and without (dotted) the neck degree of freedom for several representative elements from the ^{197}Au + 401 MeV ^{56}Fe reaction.

Fig. 19. A comparison between experimental (symbols) and calculated (curves) c.m. angular distributions for several representative elements from the ^{107,109}Ag + 470 MeV ^{56}Fe reaction.

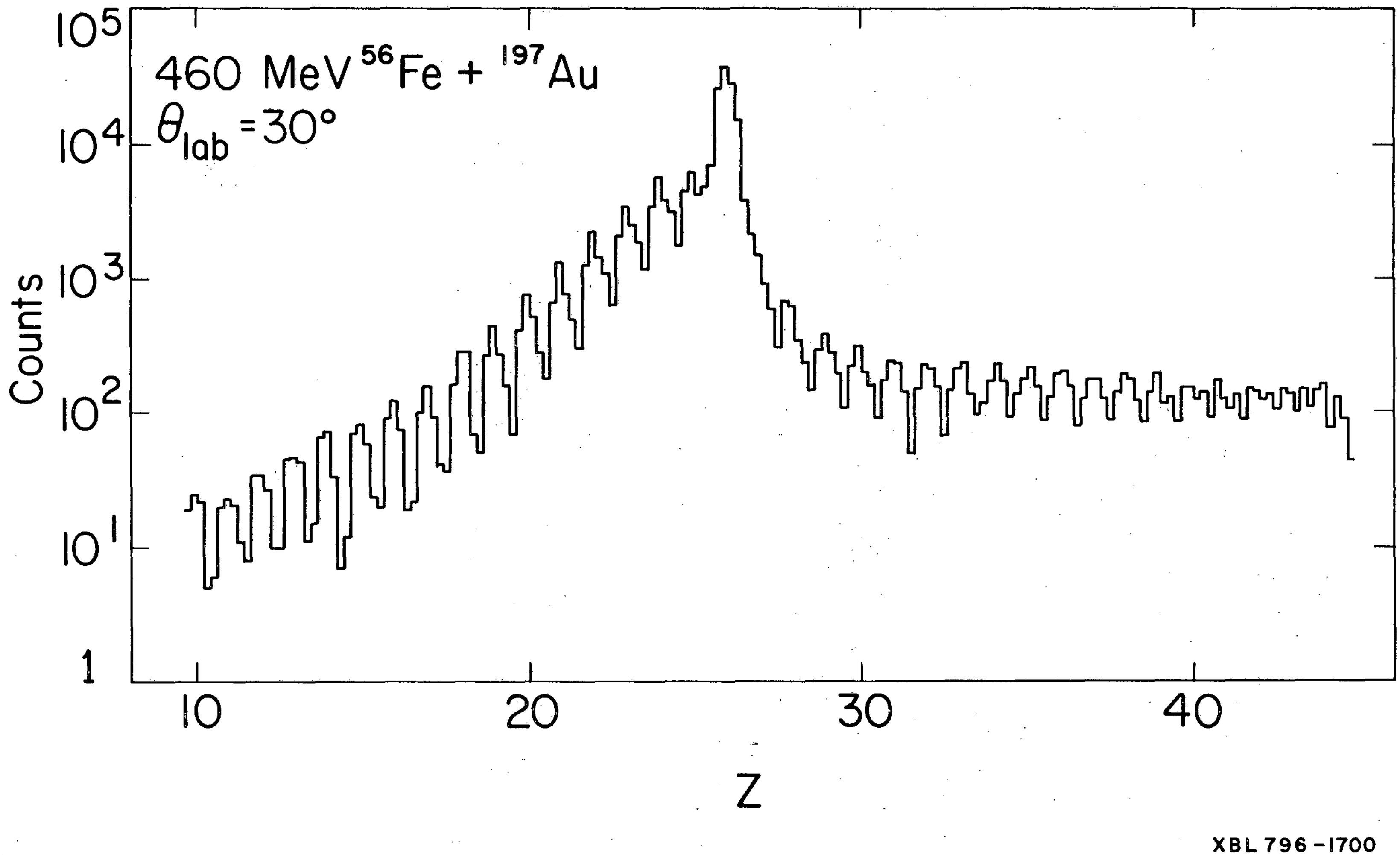
460 MeV 56Fe + 197Au
θlab =30°
Counts
10^5
10^4
10^3
10^2
10^1
1
10
20
30
40
Z
XBL 796-1700

Fig. 1

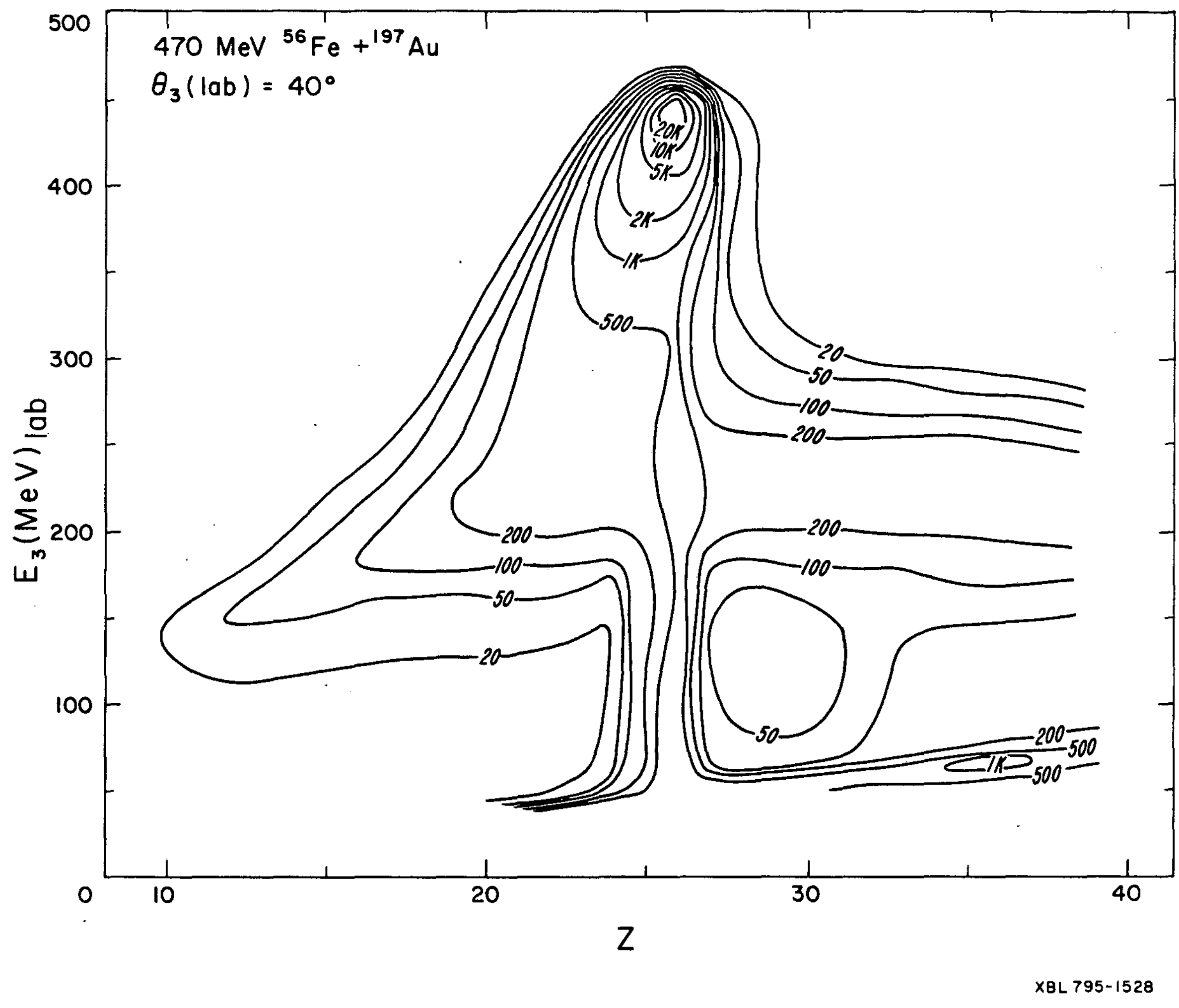
470 MeV 56Fe +197Au
θ3(lab) = 40°
E3(MeV)lab
Z
20K
10K
5K
2K
1K
500
200
100
50
20
0
10
20
30
40
100
200
300
400
500
XBL 795-1528

Fig. 2

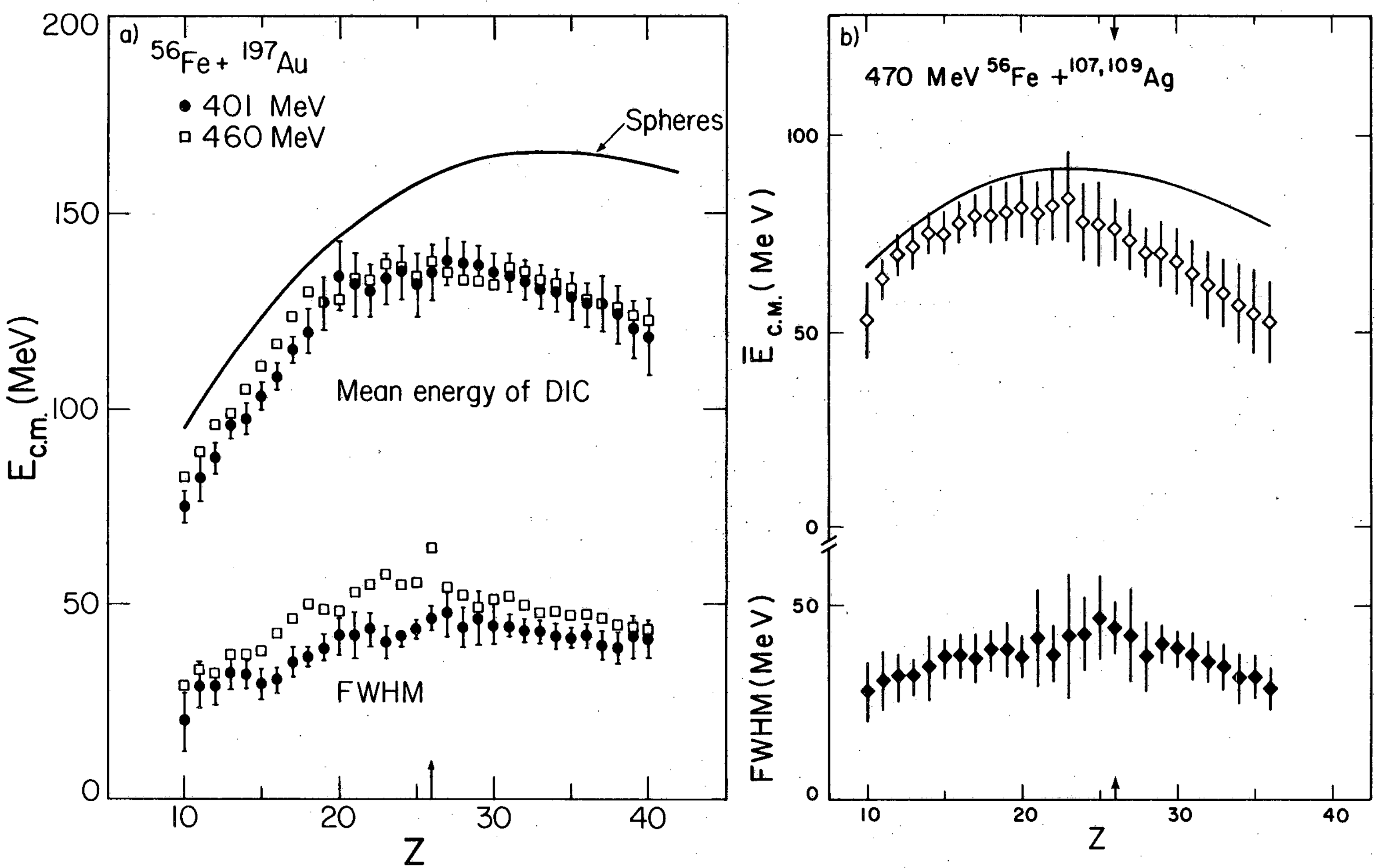

XBL 796-1703A

Fig. 3

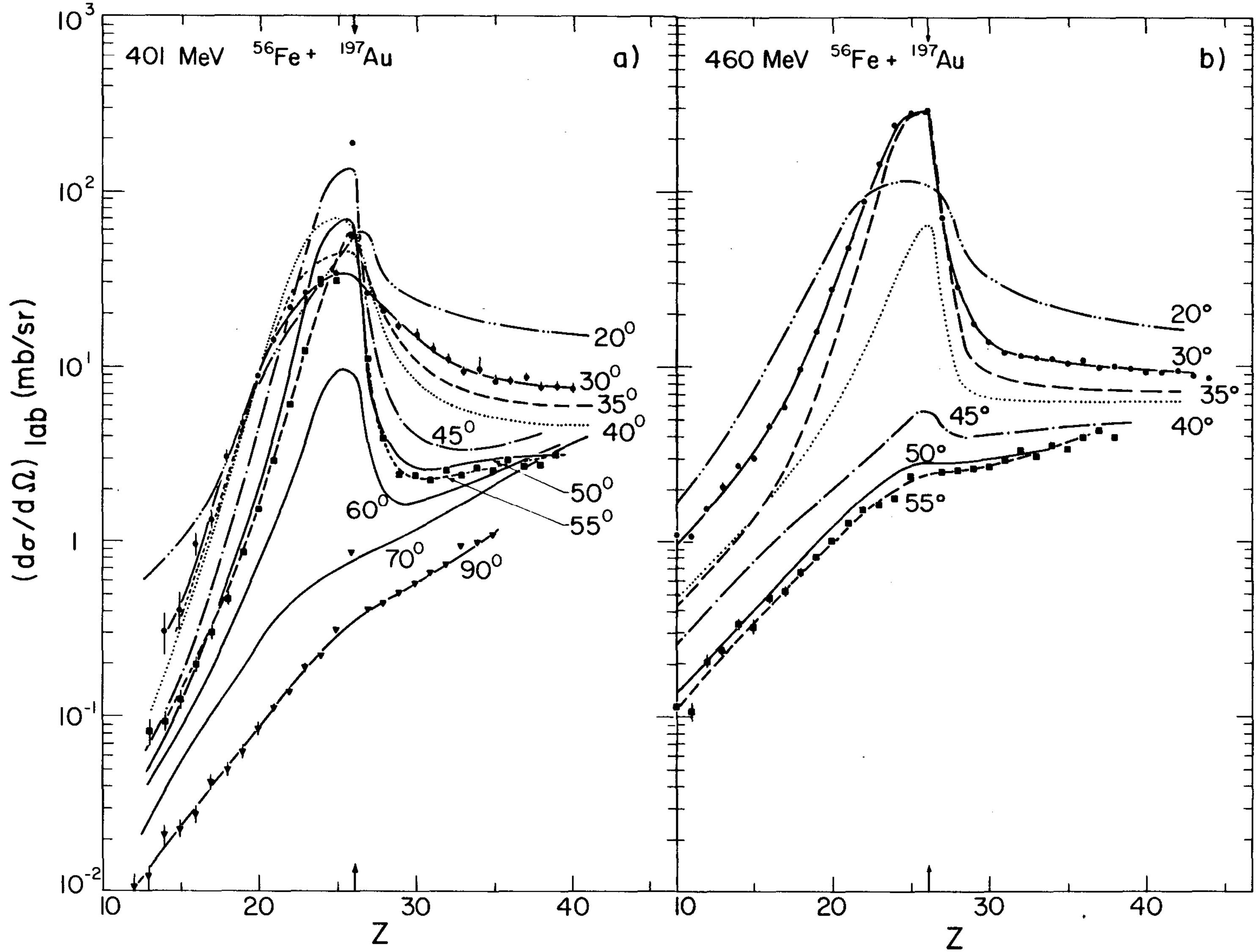
401 MeV ^{56}Fe + ^{197}Au
a)
460 MeV ^{56}Fe + ^{197}Au
b)
$(d\sigma/d\Omega)_{lab}$ (mb/sr)
Z
20°
30°
35°
40°
45°
50°
55°
60°
70°
90°
XBL 795-1415A

Fig. 4

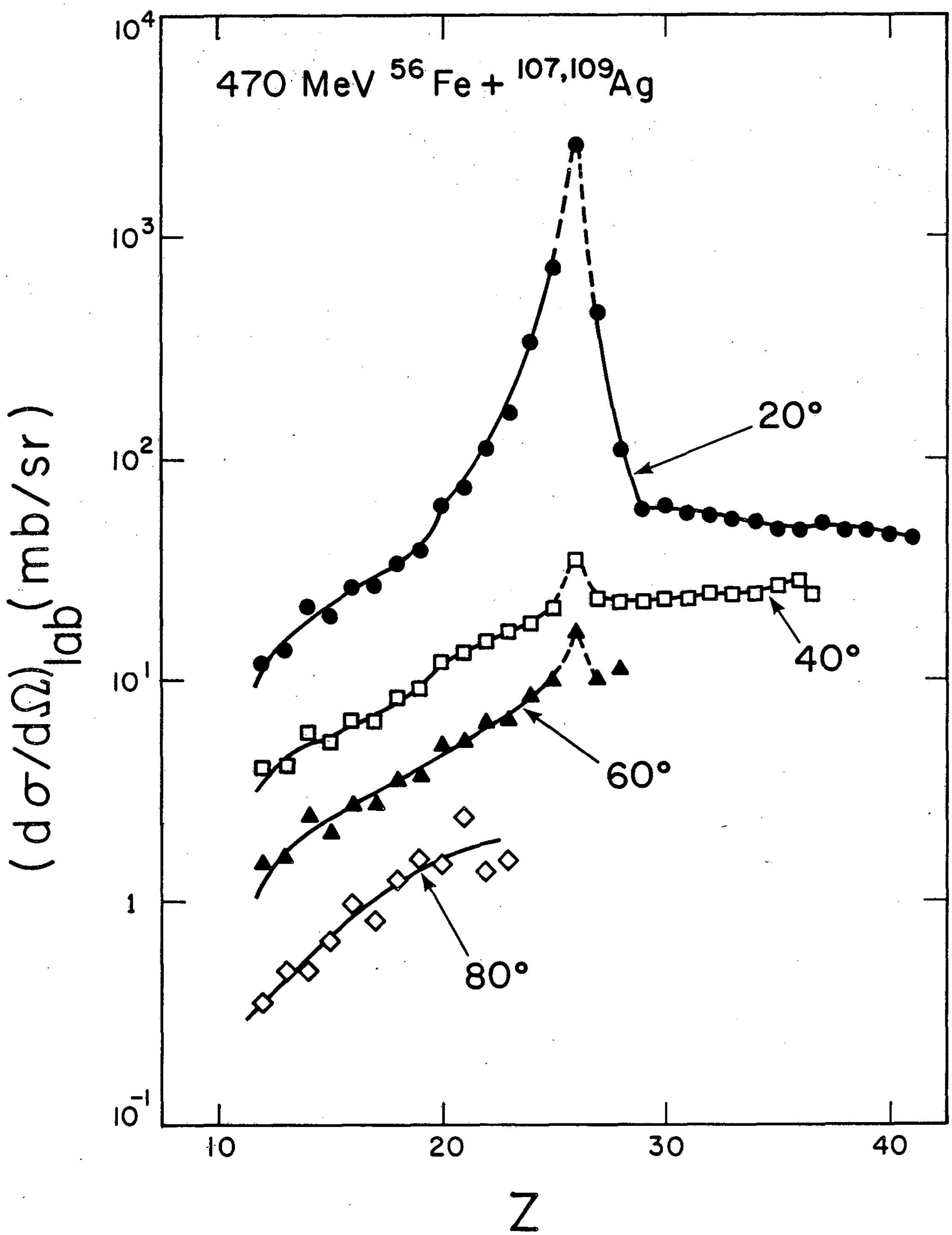

XBL 796-1702

Fig. 5

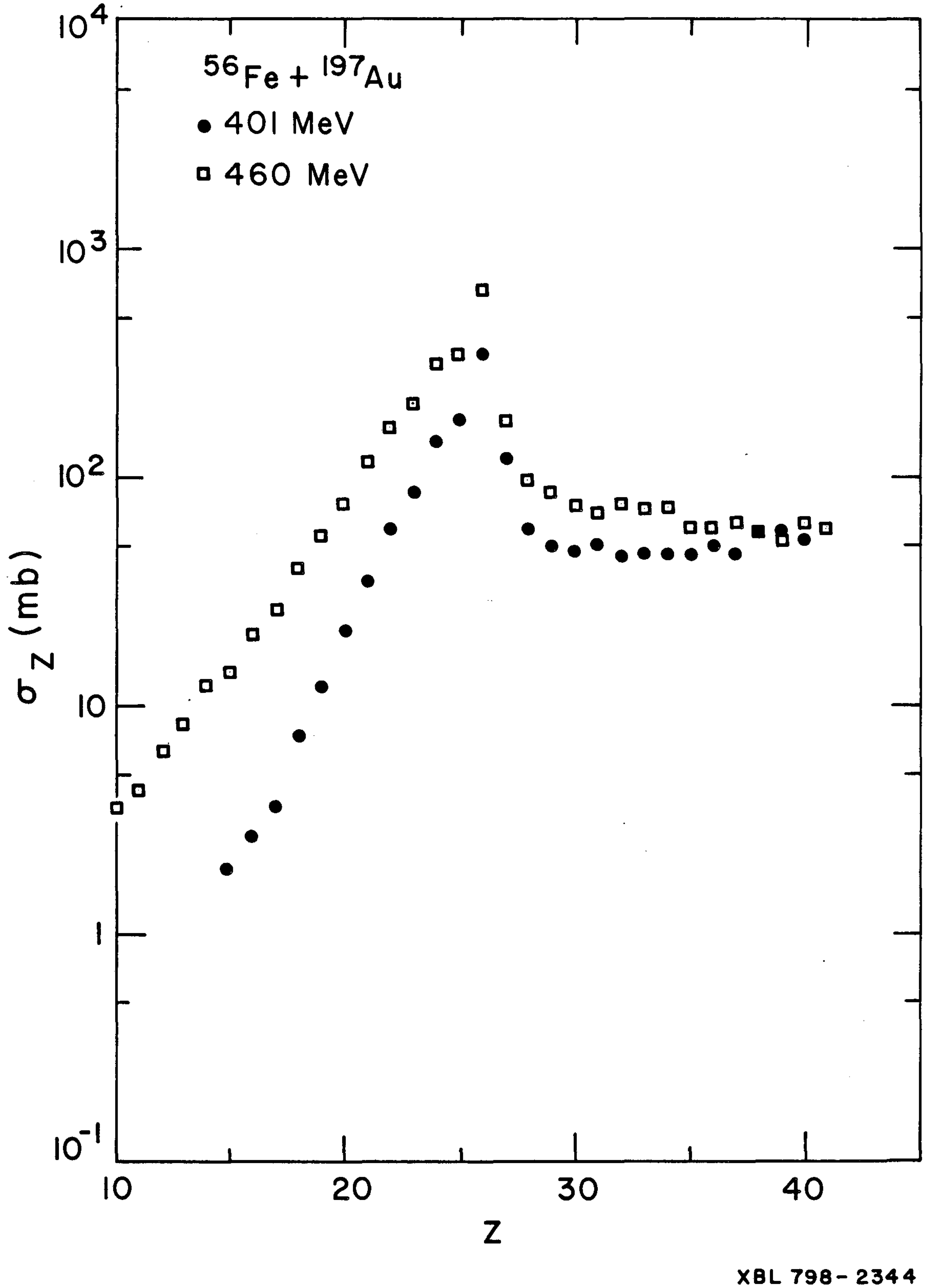

$^{56}Fe + ^{197}Au$
● 401 MeV
□ 460 MeV
10^4
10^3
10^2
10
1
10^{-1}
σ_Z (mb)
10
20
30
40
Z
XBL 798-2344

Fig. 6

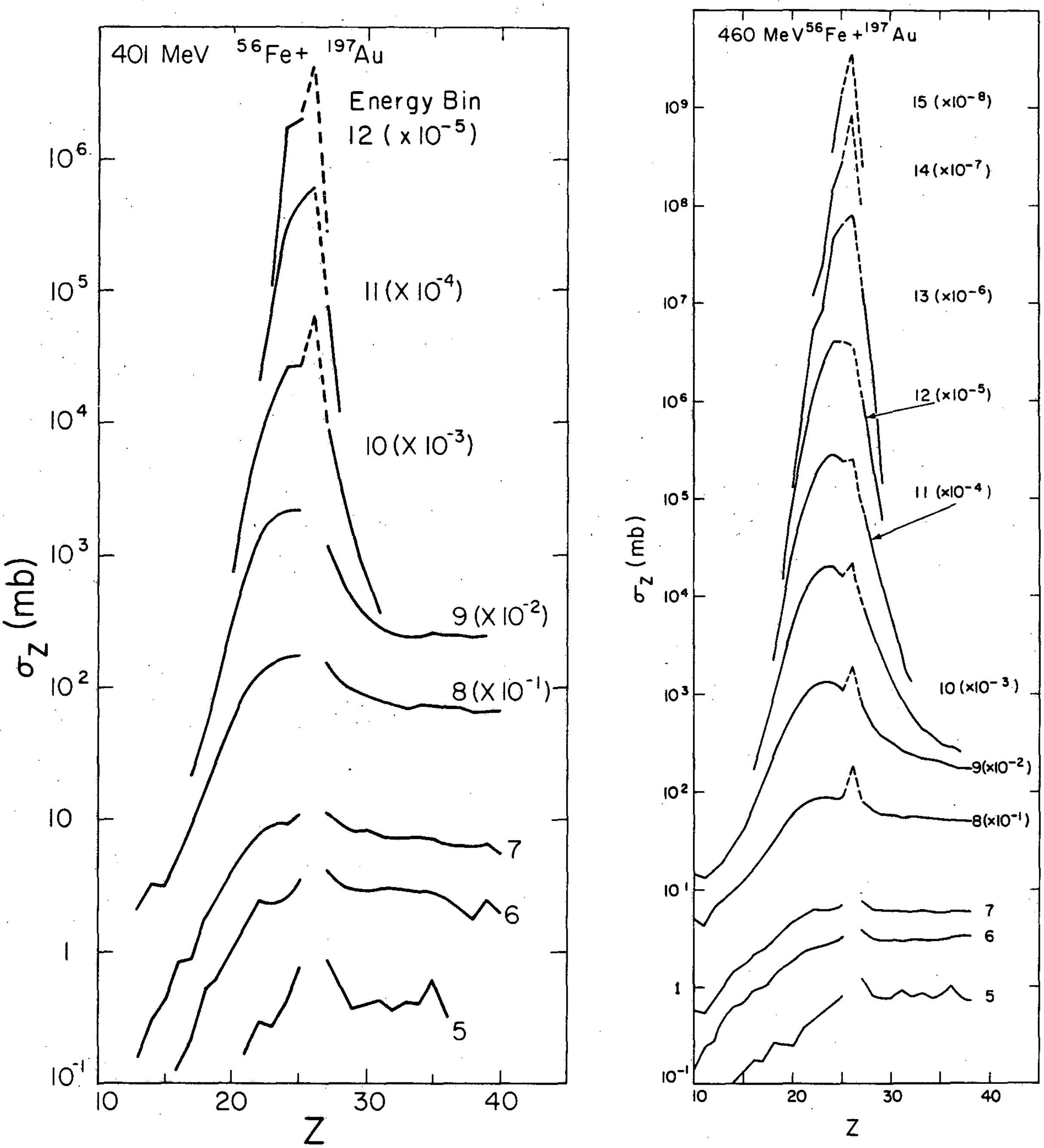

XBL 795-1526A

Fig. 7

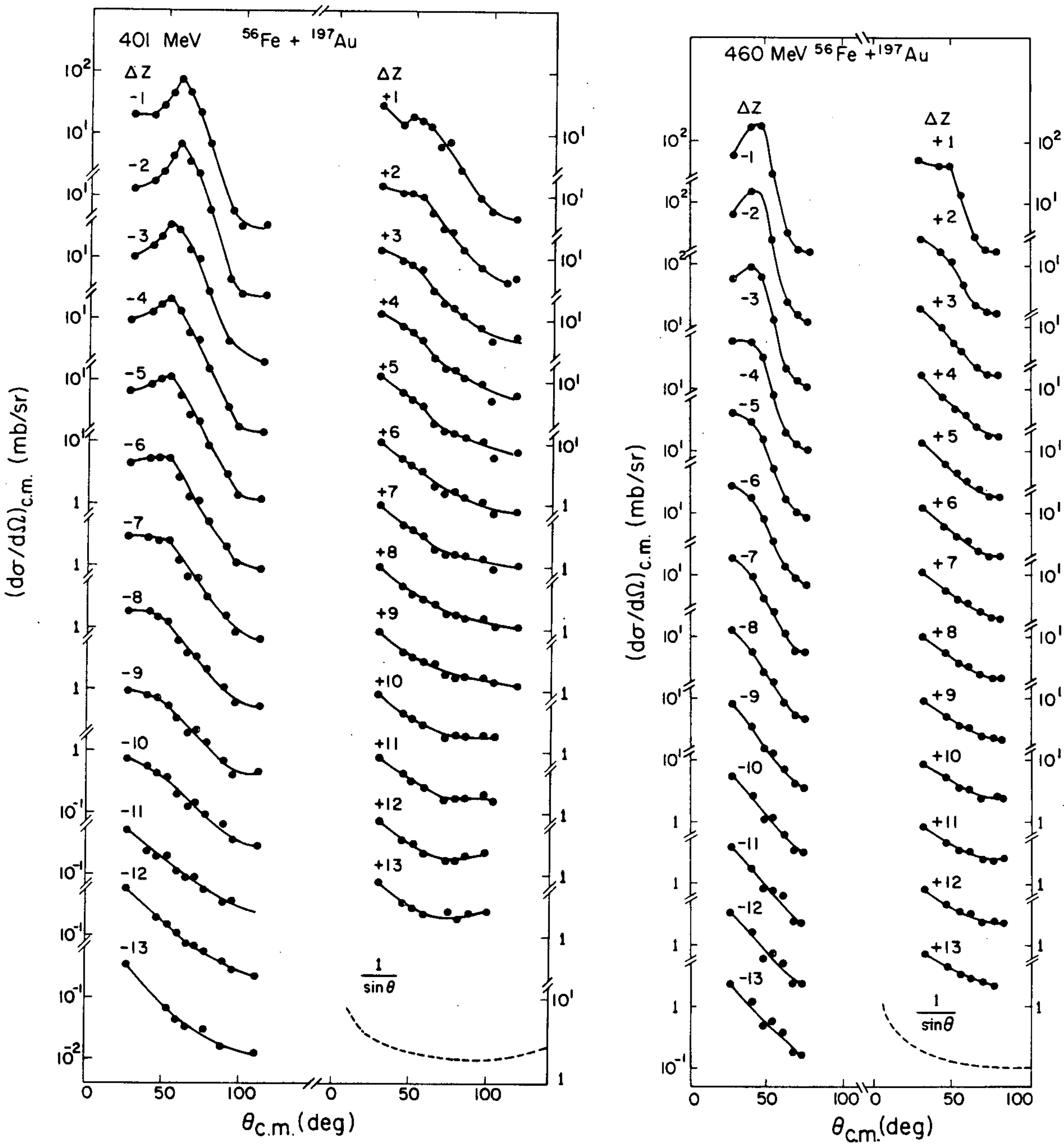

XBL 795-9723A

Fig. 8

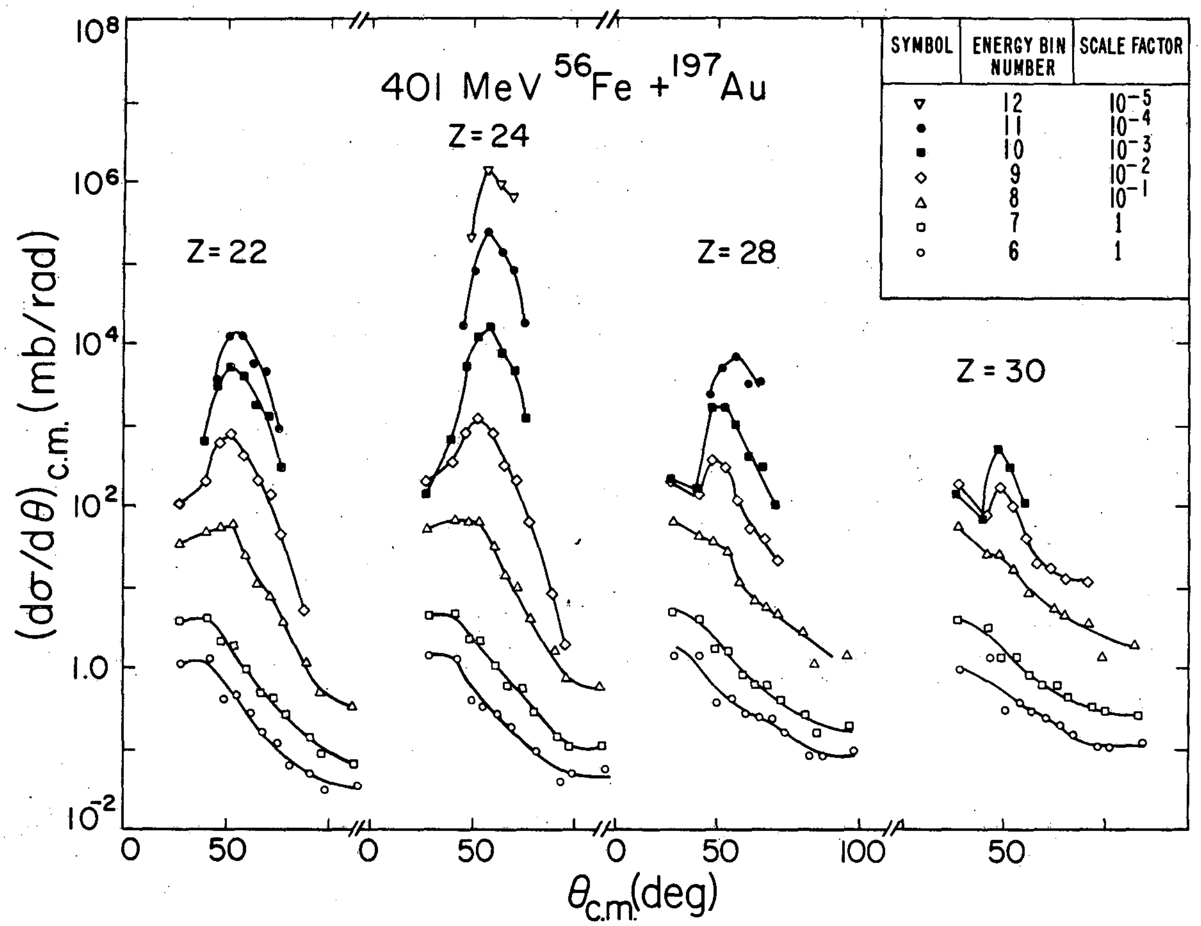
401 MeV $^{56}Fe + ^{197}Au$
Z = 22
Z = 24
Z = 28
Z = 30
SYMBOL
ENERGY BIN NUMBER
SCALE FACTOR
12 10^{-5}
11 10^{-4}
10 10^{-3}
9 10^{-2}
8 10^{-1}
7 1
6 1
$(d\sigma/d\theta)_{c.m.}$ (mb/rad)
$\theta_{c.m.}$(deg)
10^{8}
10^{6}
10^{4}
10^{2}
1.0
10^{-2}
0
50
100
XBL 795-1413

Fig. 9

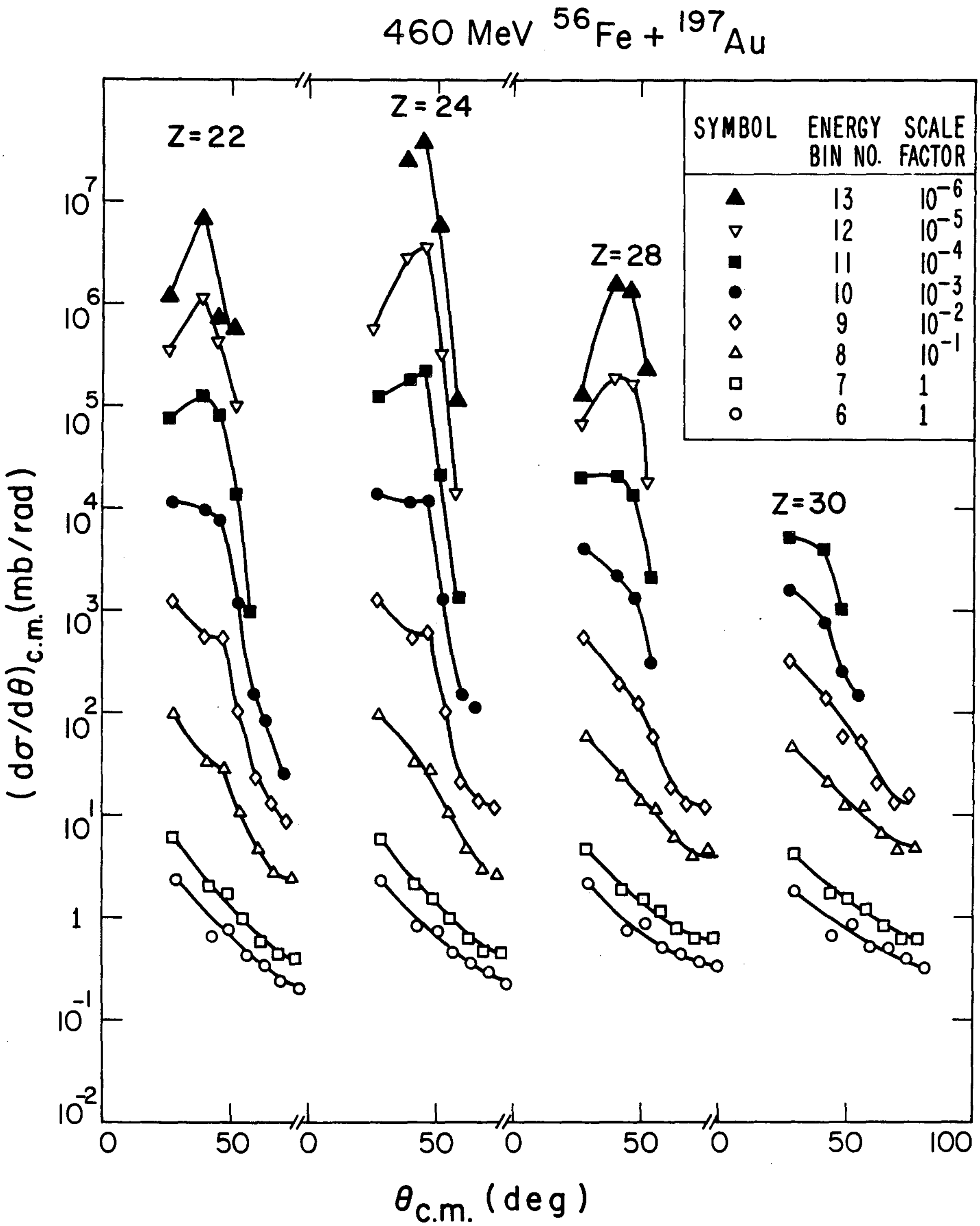

XBL 795-1554

Fig. 10

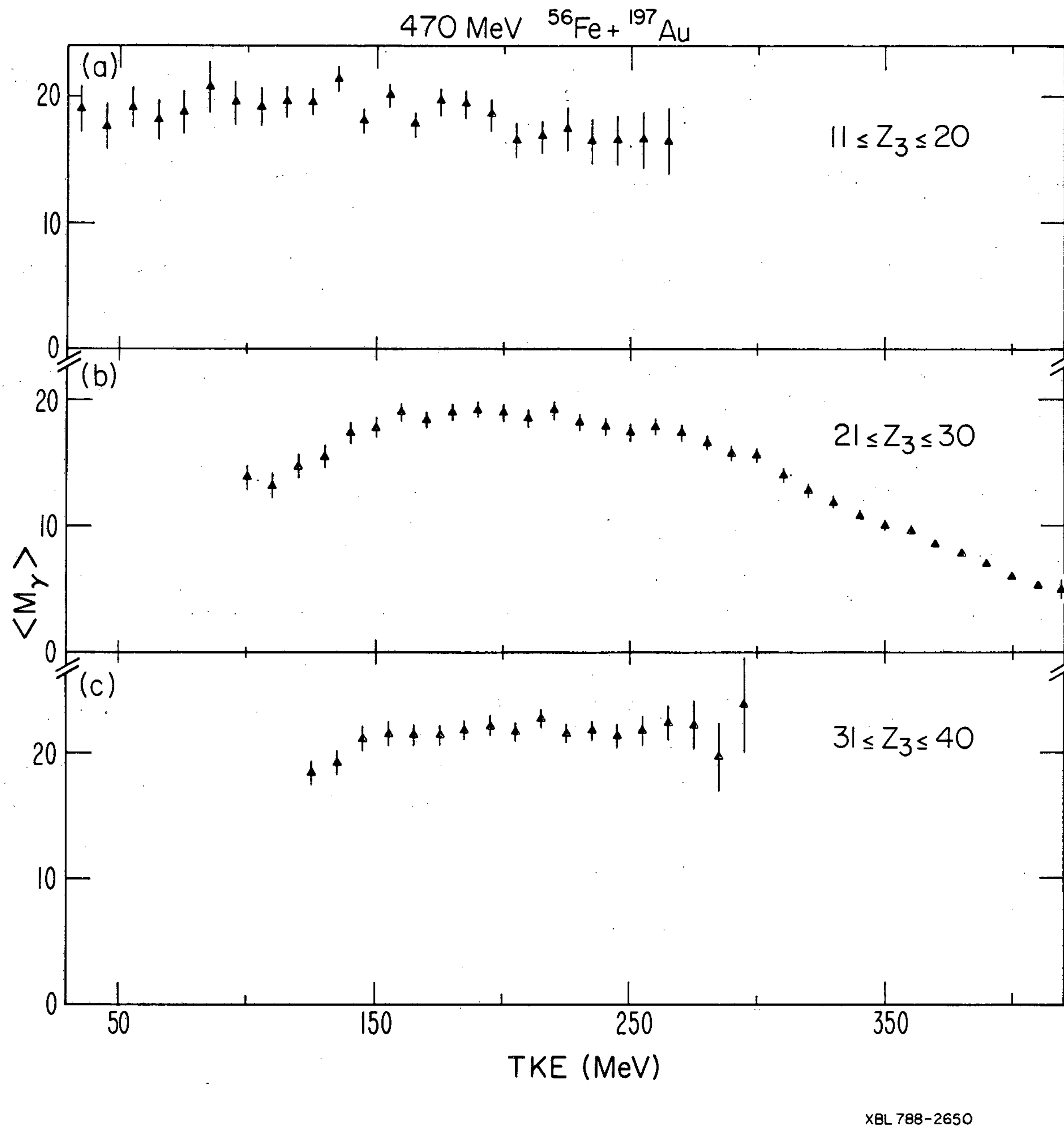
470 MeV ^{56}Fe + ^{197}Au
(a)
11 ≤ Z3 ≤ 20
(b)
21 ≤ Z3 ≤ 30
(c)
31 ≤ Z3 ≤ 40
<Mγ>
0
10
20
50
150
250
350
TKE (MeV)
XBL 788-2650

Fig. 11

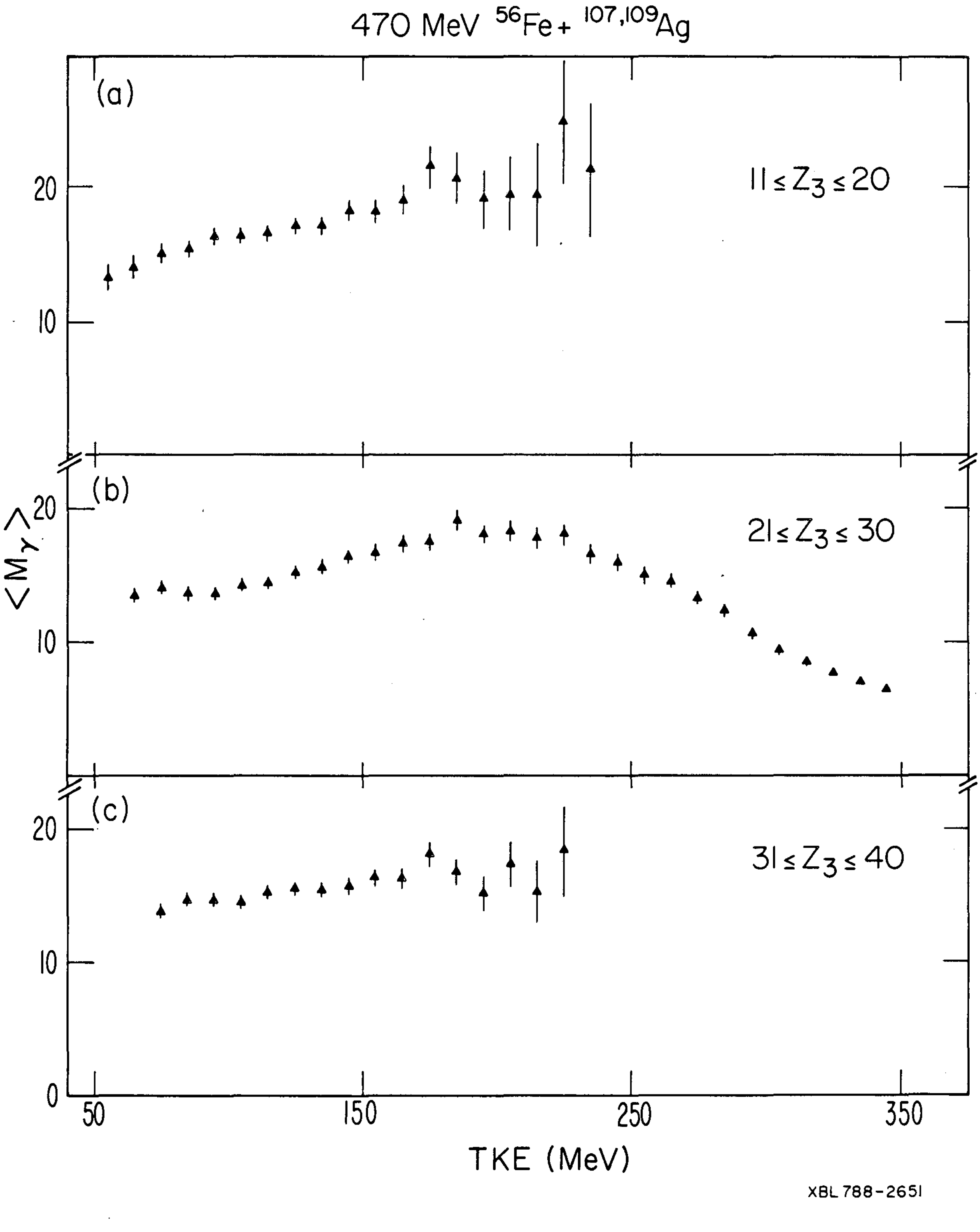
470 MeV ^{56}Fe + ^{107,109}Ag
(a)
11 ≤ Z_3 ≤ 20
(b)
21 ≤ Z_3 ≤ 30
(c)
31 ≤ Z_3 ≤ 40
<M_γ>
20
10
0
50
150
250
350
TKE (MeV)
XBL 788-2651

Fig. 12

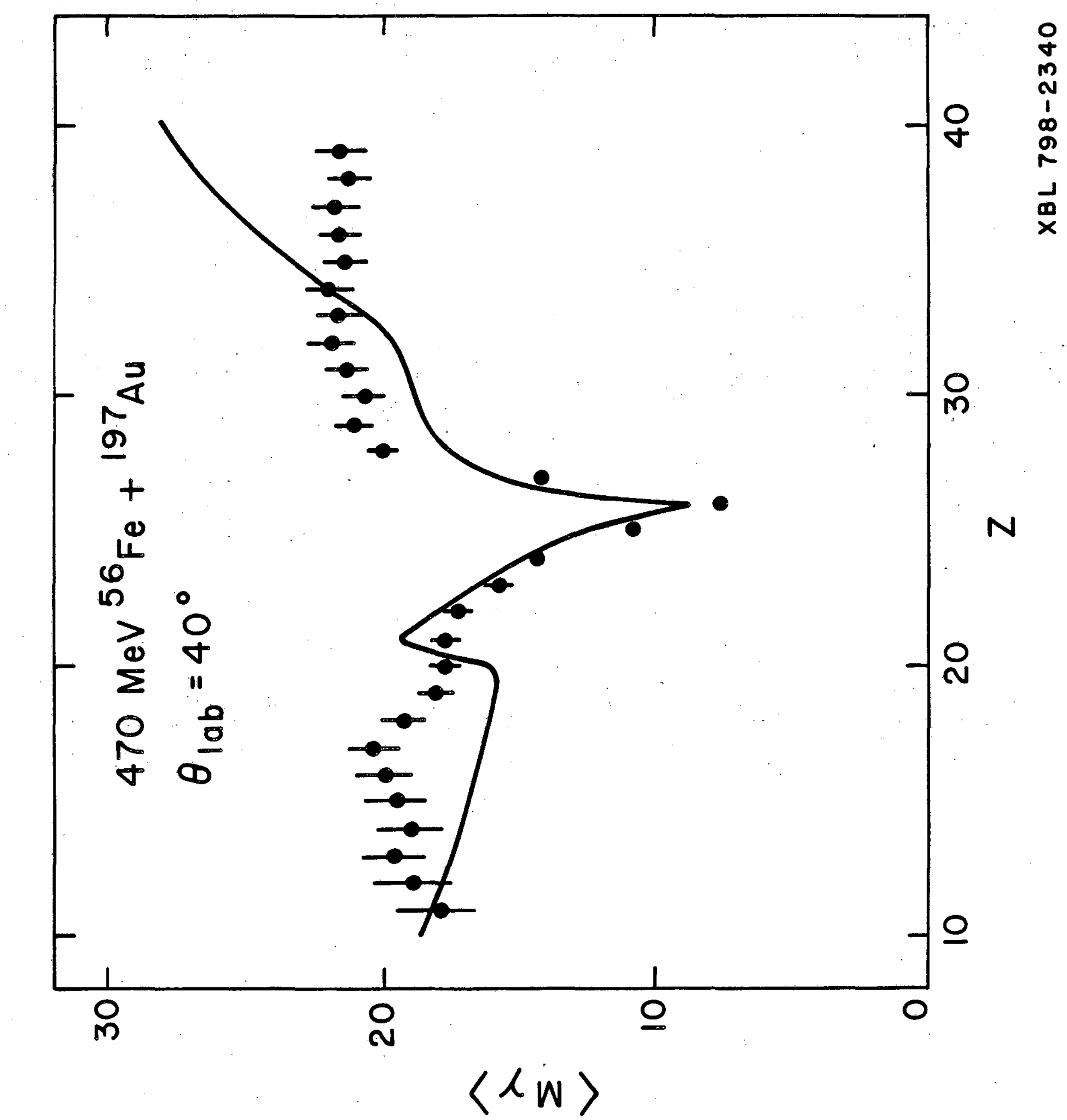
470 MeV ^{56}Fe + ^{197}Au
$\theta_{lab} = 40°$
⟨Mγ⟩
Z
0
10
20
30
10
20
30
40
XBL 798-2340

Fig. 13

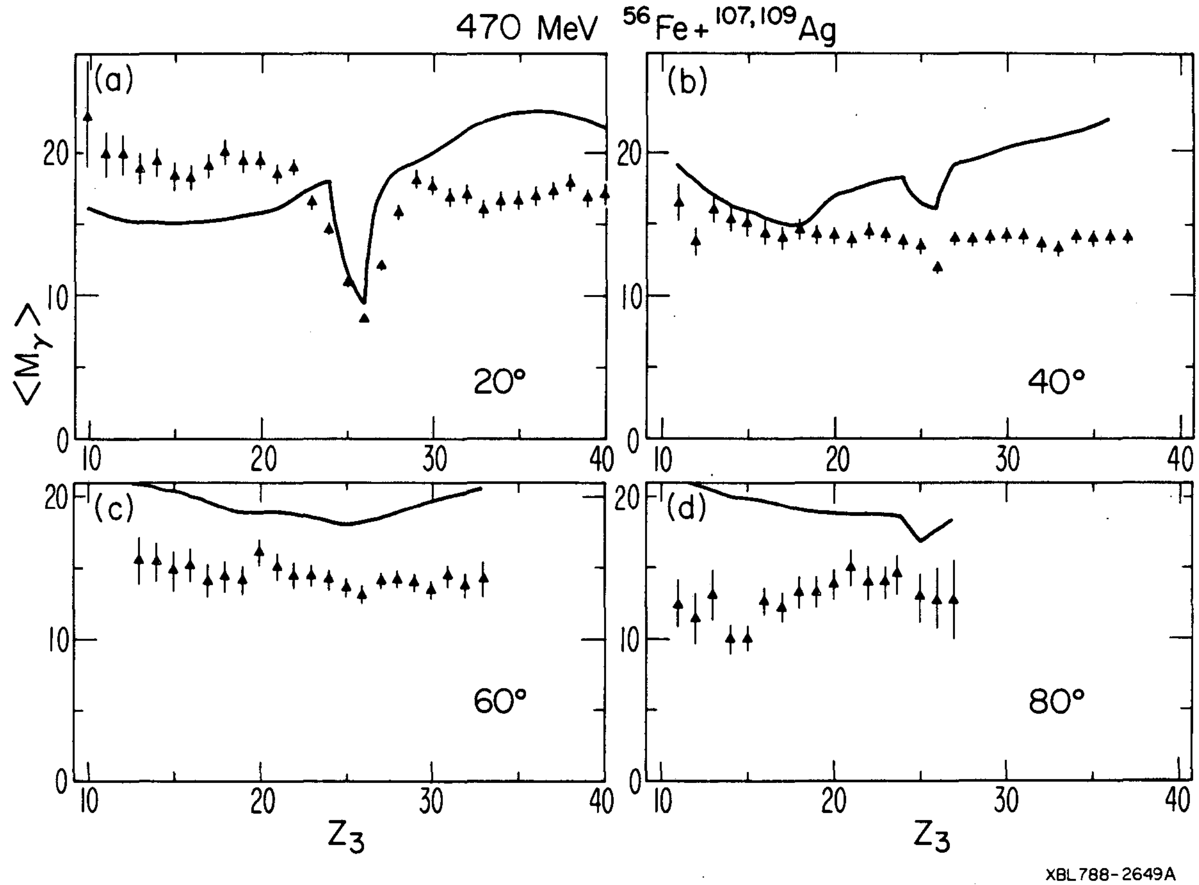
470 MeV $^{56}Fe + ^{107,109}Ag$
(a)
(b)
(c)
(d)
20°
40°
60°
80°
$\langle M_\gamma \rangle$
Z_3
Z_3
XBL 788-2649A

Fig. 14

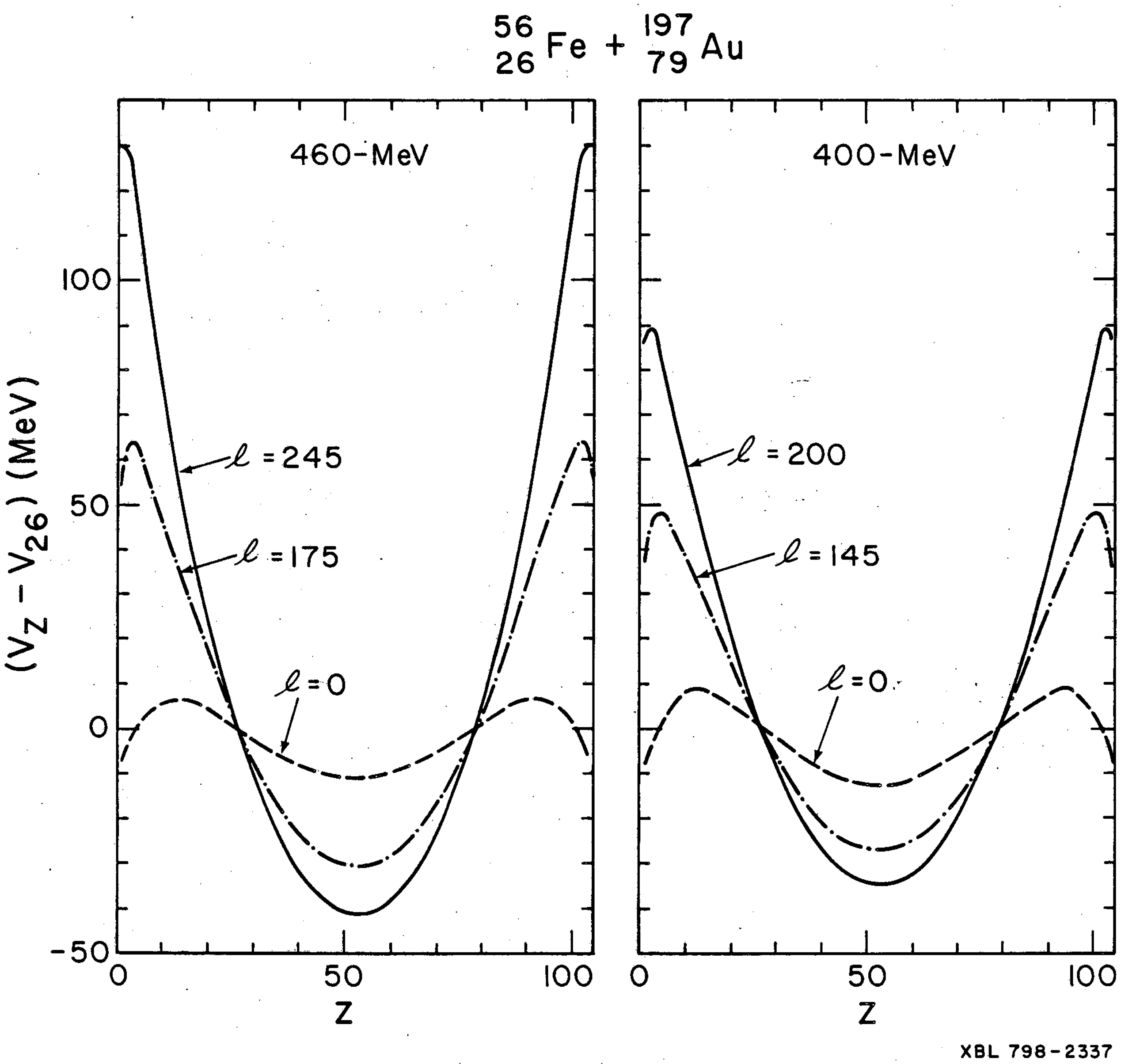

$^{56}_{26}$Fe + $^{197}_{79}$Au
460-MeV
400-MeV
ℓ = 245
ℓ = 175
ℓ = 0
ℓ = 200
ℓ = 145
ℓ = 0
$(V_Z - V_{26})$ (MeV)
100
50
0
-50
0
50
100
Z
0
50
100
Z
XBL 798-2337

Fig. 15

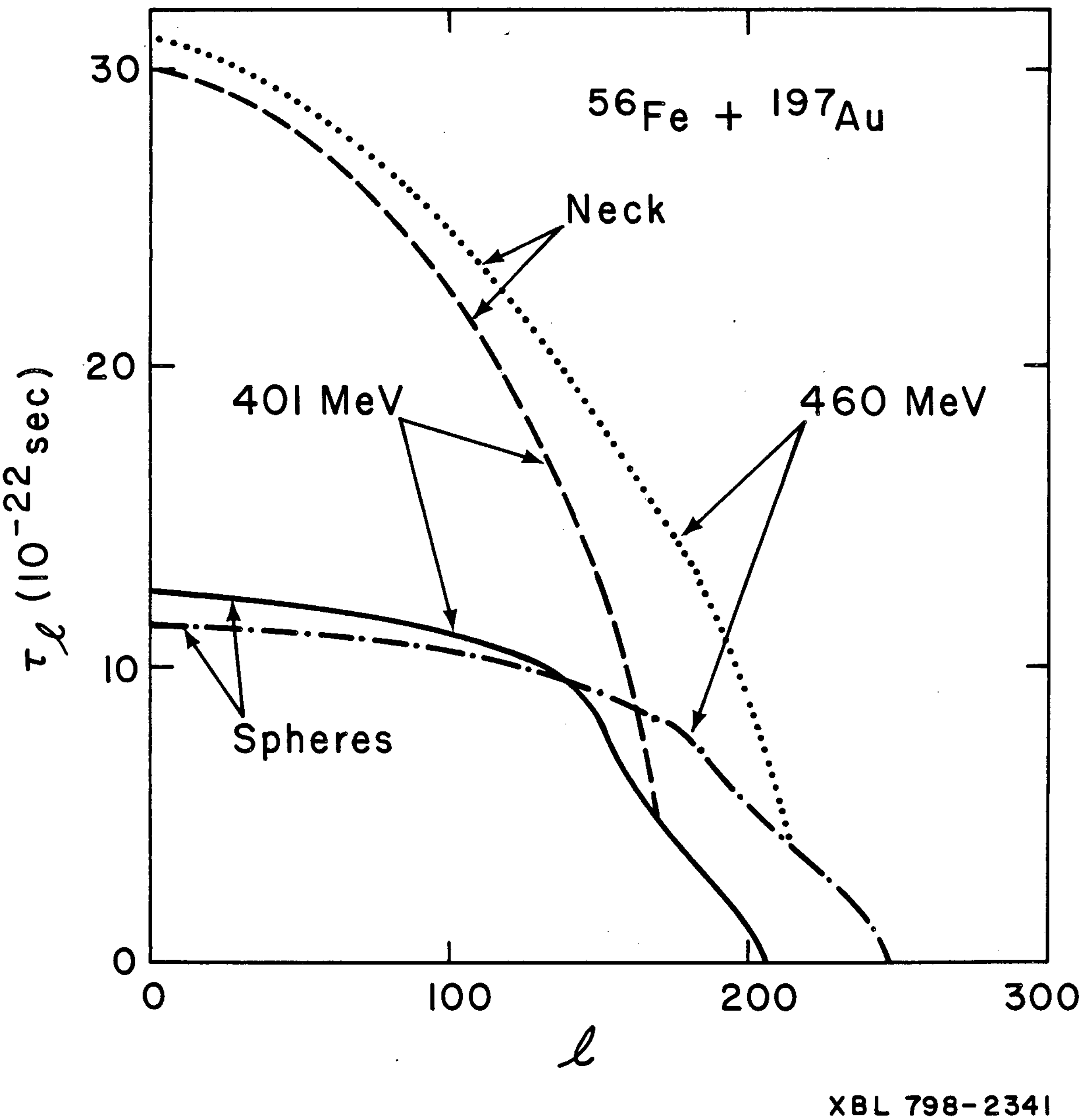

$^{56}Fe + ^{197}Au$
Neck
401 MeV
460 MeV
Spheres
τ_ℓ (10^{-22} sec)
ℓ
0
10
20
30
0
100
200
300
XBL 798-2341

Fig. 16

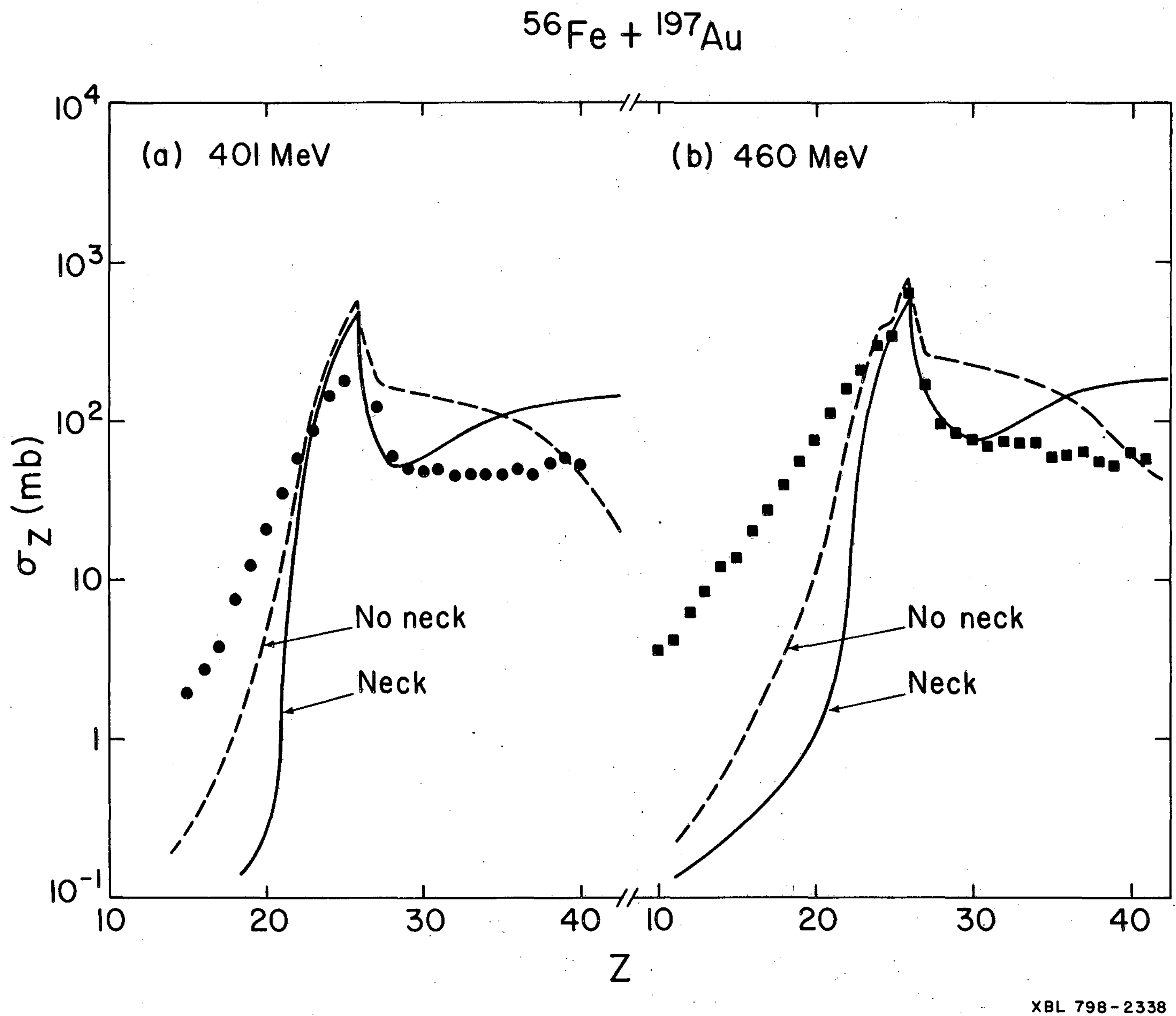

⁵⁶Fe + ¹⁹⁷Au
(a) 401 MeV
(b) 460 MeV
No neck
Neck
No neck
Neck
σ_Z (mb)
Z
XBL 798-2338

Fig. 17

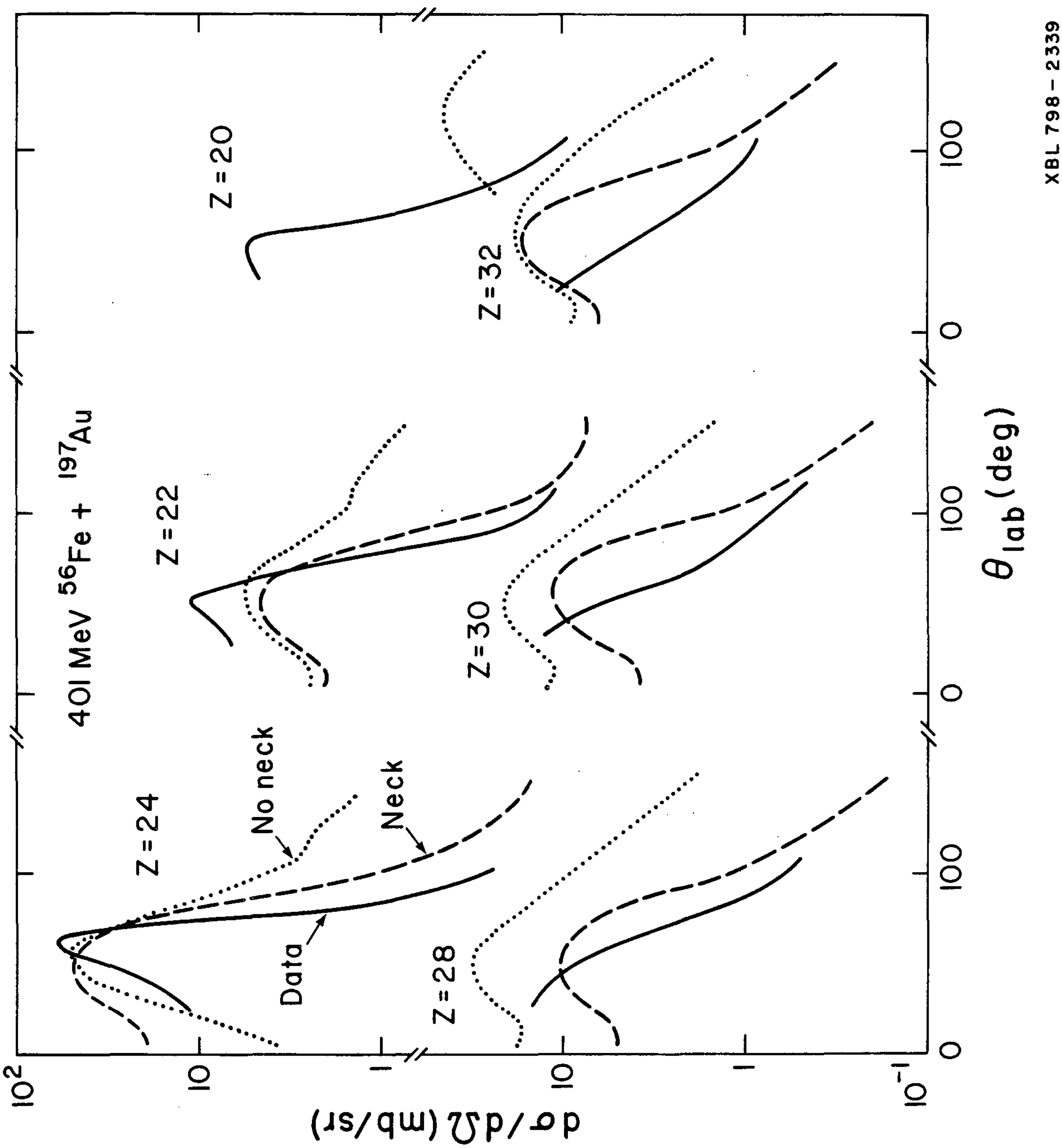

401 MeV 56Fe + 197Au
Z = 24
Z = 22
Z = 20
Z = 28
Z = 30
Z = 32
No neck
Neck
Data
dσ/dΩ (mb/sr)
θlab (deg)
10²
10
1
10
1
10⁻¹
0
100
0
100
0
100
XBL 798 - 2339

Fig. 18

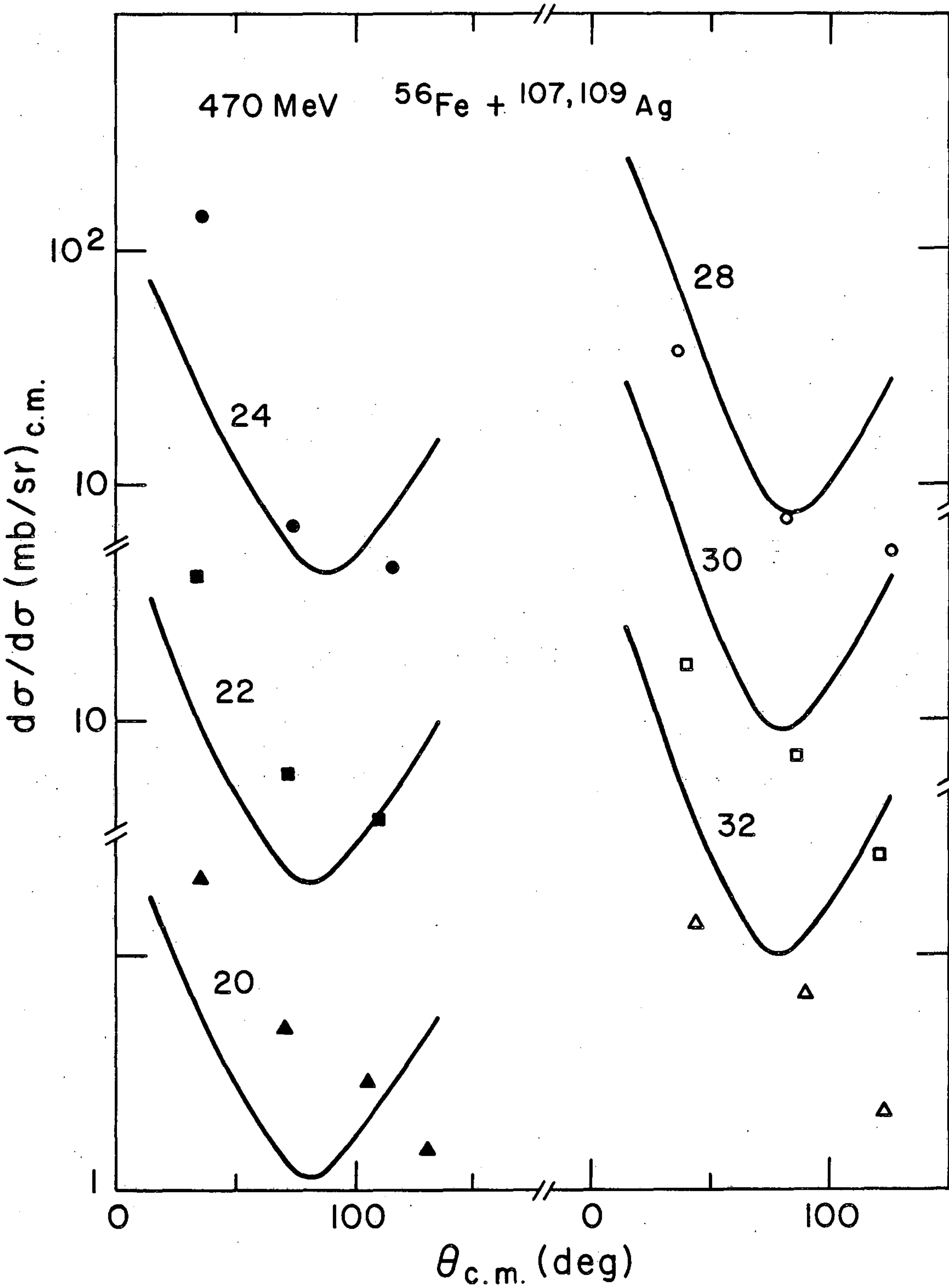
470 MeV $^{56}Fe + ^{107,109}Ag$
$d\sigma/d\sigma$ (mb/sr)c.m.
10^2
10
10
1
24
22
20
28
30
32
0
100
0
100
$\theta_{c.m.}$ (deg)
XBL 798-2342

Fig. 19

TECHNICAL INFORMATION DEPARTMENT
LAWRENCE BERKELEY LABORATORY
UNIVERSITY OF CALIFORNIA
BERKELEY, CALIFORNIA 94720